

Role of Star-Planet Interactions in the Observed X-ray Activity of HD179949

Anshuman Acharya

A dissertation submitted for the partial fulfilment of BS-MS

Dual Degree in Science, at IISER Mohali



**Indian Institute of Science Education and Research,
Mohali**

April 2021


Certificate of Examination

This is to certify that the dissertation titled Role of **Star-Planet Interactions in the Observed X-ray Activity of HD179949** submitted by **Anshuman Acharya** (Reg. No. MS16080) for the partial fulfillment of BS- MS Dual Degree programme of the institute, has been examined by the thesis committee duly appointed by the institute. The committee finds the work done by the candidate satisfactory and recommends that the report be accepted.

Prof. Jasjeet S. Bagla

 28/04/2021

Dr. Aru Beri

 28/4/2021
Dr. Anosh Joseph


Apr 28 2021

Dr. Vinay Kashyap
(Supervisor)

 28.04.2021

Prof. Kulinder P. Singh
(Co-Supervisor)

Dated: April 9th, 2021

Declaration

The work presented in this dissertation has been carried out by me under the guidance of Dr. Vinay Kashyap at the Smithsonian Astrophysical Observatory, Harvard & Smithsonian and Prof. Kulinder Pal Singh at the Indian Institute of Science Education and Research, Mohali.

This work has not been submitted in part or in full for a degree, a diploma, or a fellowship to any other university or institute. Whenever contributions of others are involved, every effort is made to indicate this clearly, with due acknowledgement of collaborative research and discussions. This thesis is a bonafide record of original work done by me and all sources listed within have been detailed in the bibliography.

Anshuman Acharya
(Candidate)

Dated: 9th April, 2021

In my capacity as the supervisor of the candidates project work, I certify that the above statements by the candidate are true to the best of my knowledge.

KPSingh 28.04.2021
Prof. Kulinder Pal Singh
(Supervisor)

Acknowledgements

This academic year (2020-21) has been unprecedented for everyone due to the pandemic. I am deeply thankful to my supervisor Dr. Vinay Kashyap for letting me to work with him remotely. Despite the cancellation of my travel plans to the Smithsonian Astrophysical Observatory (SAO), Center for Astrophysics | Harvard & Smithsonian, we were successfully able to work on this project through regular interactions through videoconferencing, emails and written logs on Google Docs. The techniques, methodologies and physics I was able to learn from him has been an amazing experience for me. I am also deeply thankful to his patience in dealing with the multitude of doubts I approached him with, as well as for adjusting his schedule to manage with the timezone differences. I am also extremely grateful to my local supervisor, Prof. Kulinder Pal Singh, whose meticulousness and experience has allowed me to improve my approach of doing as well as explaining science. His assistance in facilitating interactions with Dr. Kashyap, and suggestions on resources I could use made this project possible despite no in-person interactions.

I would also like to thank the mentors I have had through my journey over my undergraduate years. Prof. Shankar Ghosh, Prof. Robert Antonucci, Dr. Vikram Khairé, Prof. Andreas Just and Branislav Avramov as mentors for various projects played a crucial role in developing my love and understanding for science in general and astronomy in particular. I am also deeply thankful to Prof. Jasjeet Singh Bagla whose suggestions and advice has helped me chart my journey over the 5 years at IISER Mohali.

Further, I am deeply thankful to my parents, who have taken care of me, and kept me safe, as I spent the entire year at home. Dealing with the reality of the pandemic while keeping me shielded from its repercussions and reality must have required immense amounts of strength and fortitude. I am glad to have had them by my side during this period. Lastly, but definitely not the least, I am thankful to my friends Abhijit Bhalachandra, Rahul Ramesh and Rishi Gangadhar, whose daily conference calls allowed me to maintain my sanity. Their suggestions to deal with problems I was stuck with, jokes to lighten the mood, and discussions on a wide array of topics was a welcome refresher. I am glad that my best memories of college were made with them.

Lastly, I would like to thank the IISER Mohali administration for allowing me to spend my last few months on-campus with my friends, and taking appropriate precautions to make living on-campus relatively safe.

List of Figures

1.1	Artistic depiction of SPI created by Antoine Stugarek, University of Montréal.	2
2.1	The Chandra X-ray Observatory is the world's most powerful X-ray telescope. It has eight-times greater resolution and is able to detect sources more than 20-times fainter than any previous X-ray telescope. <i>Credits: NASA/CXC & J.Vaughan</i>	6
2.2	Image of HD179949 with the “PM corrected position” marker showing the measured position after taking proper motion into account, while the “SIMBAD position” marker shows the expected position from SIMBAD. The inner circle marked as the “Circle for Centroid” has a 2” radius and is used for centroiding. The outer circle marked as “Circle for Source Counts” has a 3.6” radius and is used to get the total number of counts from the source.	9
2.3	Left: Image in CHIP coordinates with CCD ID = 7 and Right: Image in SKY coordinates	9
3.1	Corner Plot showcasing results from MCMC draws using the pyBLoCXS package for observation ID 6120. The error bars are showcased by the 16th to 84th percentile range dashed lines (left and right most for each parameter) and the accepted value is the 50th percentile value given by the central dashed line.	18
3.2	For observation ID 6120: Top Left: Spectral fit for Model A; Top Right: Spectral fit for Model B. Bottom Left: Spectral fit for Model C. Bottom Right: Spectral fit for Model D.	20
3.3	For observation ID 6121: Top Left: Spectral fit for Model A; Top Right: Spectral fit for Model B. Bottom Left: Spectral fit for Model C. Bottom Right: Spectral fit for Model D.	21
3.4	Cumulative sum test for the 4 models for observation ID 6120.	22
3.5	Cumulative sum test for the 4 models for observation ID 6121.	22
3.6	Flux versus Time for the Chandra, XMM-Newton and <i>Swift</i> observations.	23

3.7	Flux versus Phase for the Chandra, XMM-Newton and <i>Swift</i> observations, with running mean for N=4 shown.	24
3.8	Lomb-Scargle periodogram, window function, and the subtracted periodogram for the observed spectral fluxes versus time.	25
3.9	Count rates in each passband across all Chandra observation IDs. The grey bars show the exposure duration of each observation.	26
3.10	Overall light curve in the broad pass band 0.5-7.0 keV with respect to the orbital phase of the planet HD 179949b for observation ID 5427.	27
3.11	Light curve with optimal binning versus phase for the physically motivated passbands.	29
3.12	Light curve with optimal binning versus phase for the Chandra passbands. .	29
3.13	Hardness Ratio (HR) graphs for the Fe1718 and bandMg (including Silicon, Aluminium and Sulphur) pass bands for the observation IDs 5427 and 6119. .	32
3.14	Hardness Ratio (HR) graphs for the Fe1718 and bandMg (including Silicon, Aluminium and Sulphur) pass bands for the observation IDs 6120 and 6121. .	33
3.15	Hardness Ratio (HR) graphs for the Fe1718 and bandMg (including Silicon, Aluminium and Sulphur) pass bands for the observation IDs 6122.	34
3.16	Hardness Ratio (HR) graphs for the Fe1718 and bandNe pass bands for the observation IDs 5427 and 6119.	35
3.17	Hardness Ratio (HR) graphs for the Fe1718 and bandNe pass bands for the observation IDs 6120 and 6121.	36
3.18	Hardness Ratio (HR) graphs for the Fe1718 and bandNe pass bands for the observation IDs 6122.	37
3.19	Hardness Ratio (HR) graphs for the Fe1718 and bandO pass bands for the observation IDs 5427 and 6119.	38
3.20	Hardness Ratio (HR) graphs for the Fe1718 and bandO pass bands for the observation IDs 6120 and 6121.	39
3.21	Hardness Ratio (HR) graphs for the Fe1718 and bandO pass bands for the observation IDs 6122. Note that as pass bands Fe1718 and bandO have the same optimal binning of 284τ , there are no graphs for translating the hard band's binning to the soft band's binning and vice-versa.	40
6.1	Color (C) graphs for the Fe1718 and bandNe pass bands for the observation IDs 5427 and 6119.	52
6.2	Color (C) graphs for the Fe1718 and bandO pass bands for observation IDs 5427 and 6119.	53

6.3	Color (C) graphs for the Fe1718 and bandMg pass bands for observation IDs 5427 and 6119.	54
6.4	Hardness Ratio (HR) and Color (C) graphs for the Soft and Ultrasoft pass bands.	55
6.5	Hardness Ratio (HR) and Color (C) graphs for the Soft and Medium + Hard pass bands.	56

Abstract

HD179949 is a Sun-like (mass of $1.23 \pm 0.01 M_{\odot}$ and radius of $1.20 \pm 0.01 R_{\odot}$) F8V main sequence star, and is a yellow-white dwarf in the Sagittarius constellation. It has a Jupiter-mass ($0.98 M_{Jupiter}$ and $1.05 R_{Jupiter}$) planet orbiting at a very close orbit of radius 0.0443 ± 0.0026 AU ([Butler 06]).

Observations and theory demonstrate that star-planet interaction (SPI) between a parent star and a close-in giant planet is a complex, yet potentially informative probe of extrasolar planetary magnetic fields. This effect could be tidal, magnetic, or a combination of both. SPI can be observed as variability in the X-ray emission from the star, typically from the outermost layers (the chromosphere, transition region and the corona, due to their proximity to the planets, low density and nonradiative heat sources). In this project, we are focusing in particular on the coronal region's ([Guedel 04]) interaction with the planet.

Because tidal and magnetic interactions fall off in magnitude at a scale of $1/d^3$ and $1/d^2$ respectively, SPI can best be observed in the tightest bound systems. HD179949b, the hot Jupiter around HD179949 is a probable candidate for observing SPI, given its orbital radius. Past observations [Gurdemir 12] and [Saar 07] of the system suggest magnetospheric interactions to be the leading cause for the variability observed. Also, in [Shkolnik 04] evidence of planet-induced heating on HD 179949 is presented. The effect lasted for over a year and peaked only once per orbit, suggesting a magnetic interaction. They suggested that these interactions could produce a chromospheric hot spot which rotates in phase with the planet's orbit, and is thus modulated by the orbital period. However, current observations show only intermittent variability rather than the expected periodicity.

[Shkolnik 07] observed synchronicity of the Ca II H & K emission with the orbit in four out of six epochs, while rotational modulation with $P_{rot} = 7$ days is apparent in the other two seasons. It further claims that if there are activity cycles, then that may be a possible explanation for the on/off nature of SPI. [Fares 12] suggests that enhancement due to magnetospheric SPIs is more likely modulated with the beat period of the system, i.e. the synodic period between the stellar rotation and the orbital period.

Thus, one of the first goals of this thesis is to determine whether there is any X-ray variability correlated with planetary phase to indicate SPI using archival data from the Chandra X-ray Observatory, and supplemented by XMM and Swift analyses from literature. If SPI

is detected, then the extent and duration of variability will be noted. Possible causes behind the variability will also be explored. The hardness ratios and colour shall be calculated for the data available to detect any softening/hardening in the spectrum which is statistically significant. Further, spectral fitting will be carried out to estimate the coronal structure and abundances.

Measuring the coronal abundances is important as it will assist us in characterising the FIP effect ([Laming 15]). Multiple spectral models will be tested, including those used for past observations (like [Scandariato 13]), to find the best possible explanation for the spectra observed. Statistical analyses of the residuals from the various fitting models will also be performed. Observations will be supplemented with results from X-ray telescopes like Swift to build up phase coverage to resolve the question of activity cycles as an explanation for the intermittency observed in [Shkolnik 07].

Contents

1	Introduction	1
2	Observations	5
2.1	Chandra X-ray Observatory	5
2.2	Data Used	6
3	Analysis	10
3.1	Spectral Fits	10
3.1.1	Spectral Flux	23
3.1.2	Lomb-Scargle Periodogram	23
3.2	Count Rates	26
3.3	Light Curves	27
3.4	Hardness Ratios	28
4	Results and Discussion	41
5	Summary	42
6	Appendix	51
A.1	Color	51
A.2	Hardness Ratios and Color for the Chandra pass bands	55

Chapter 1

Introduction

The first confirmed detection of an exoplanet occurred in 1992 ([Wolszczan 92]), and since then, the number of exoplanet detections has been going up rapidly. As of April 2021, there have been 4,704 confirmed exoplanets in 3,478 systems, with 770 systems having more than one planet ([Exoplanet.eu 21]). Due to ease of detection, giant planets are more commonly detected, although the detections are limited to planets close to the star ([Ballesteros 19]). Among these detections, Sun-like stars, are of specific interest, as they can provide us examples to compare and contrast our own Solar system with. Some of these exoplanet systems can also be observed in the X-ray regime ([Kashyap 08]).

One such giant planet system is HD 179949 which consists of an F8V main sequence star, with a close-in giant planet (hot Jupiter) revolving around it with a period of ~ 3 days. Past research suggests that star-planet interactions (SPI) may be taking place ([Viswanath 20]), which is resulting in observed enhancement of X-ray activity in the star for a limited duration. In this project, we have looked at one of the archival observations in the X-ray regime using the Advanced Imaging CCD Spectrometer (ACIS) on the Chandra X-ray Observatory, to gather evidence for or against the same.

Particularly, we have looked at the variability in X-ray emissions as a function of the phases of the planetary orbit, analysed the spectrum by finding an appropriate fitting model, measured count rates across pass bands, etc. to check if the effects of the star-planet interactions are discernible in the corona. Further, we have attempted to identify the extent of these effects, and study whether there exists a phase difference between chromospheric and coronal signatures. Past research on similar hot-Jupiter systems suggests that if tidal interactions are the cause, then the activity may vary with half the orbital period, but if magnetospheric interactions are the cause, then the variations would be noticed to vary along with the orbital period. However, [Fares 12] suggests that the SPI due to magnetospheric interactions

may also vary with the beat period of the system, which is the synodic period between the orbital period and the stellar rotation.

The star of HD 179949 is a yellow-white dwarf in the Sagittarius constellation, with a planet with mass $0.98 \pm 0.004 M_{Jupiter}$, and an orbit semi-major axis of 0.0443 ± 0.0026 AU. Other common names for the star are HIP 94645, 1RXS J191533.7-241114, HR 7291, SAO 187883, V* V5652 Sgr, Gumala, Gaia DR2 6770313530317154560, GJ 749, TYC 6875-3273-1, and HIC 94645. The properties of the star-planet system collated from different sources have been listed in Table 1.1.

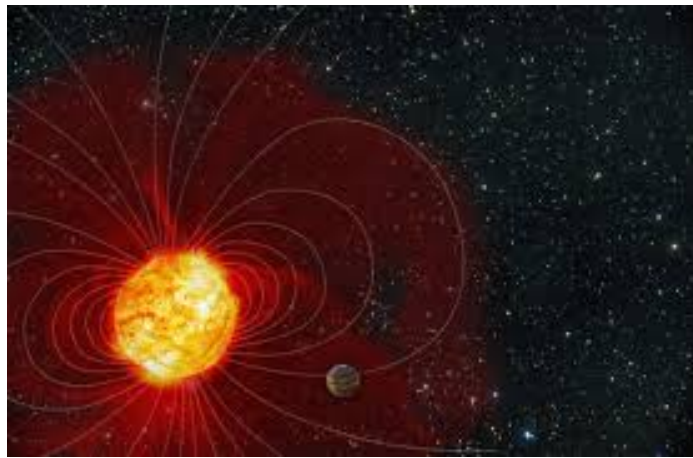


Figure 1.1: Artistic depiction of SPI created by Antoine Stugarek, University of Montréal.

Table 1.1. Properties of the HD179949 Star System:

Parameter	Value	Reference
Right Ascension	19h 15m 33.22990s (288.88846°)	Gaia DR2 ([Gaia Collaboration 18]) ^a
Declination	−24° 10′ 45.6668″ (−24.17935°)	Gaia DR2 ([Gaia Collaboration 18]) ^a
Apparent Magnitude: (V)	6.24 ± 0.01	[Høg 00] ^a
(B)	6.77 ± 0.02	
Absolute Magnitude (M _V)	4.05	XHIP ([Anderson 12]) ^a
B-V Colour Index	0.53 ± 0.03	[Høg 00] ^a
Radial Velocity	−24.619 ± 0.001 km/s	Gaia DR2 ([Soubiran, C. 18]) ^a
Proper Motion	RA +118.52 mas/yr Dec −102.235 mas/yr	Gaia DR2 [Gaia Collaboration 18] ^a
Parallax	36.39 ± 0.08 mas	Gaia DR2 [Gaia Collaboration 18] ^a
Distance	27.5 ± 0.6 pc	Gaia DR2 [Gaia Collaboration 18] ^a
Stellar Mass	1.23 ± 0.01 M_{\odot}	[Bonfanti 15]
Stellar Radius	1.20 ± 0.01 R_{\odot}	[Bonfanti 15]
Surface gravity (log g) g in cm s ^{−2}	4.36 ± 0.01	[Bonfanti 15]
Bolometric Luminosity	1.95 ± 0.01 L_{\odot}	[Bonfanti 15]
Bolometric Flux at Earth (in erg s ^{−1} cm ^{−2})	8.26 ± 0.08 × 10 ^{−8}	[Bonfanti 15]
Chromospheric Metallicity [Fe/H]	0.2226 ± 0.05 dex 0.22 ± 0.05 dex 0.137	[Gurdemir 12] [Wittenmyer 08] [Butler 06]
Photospheric Temperature	6220 ± 28 K	[Bonfanti 15]
Age	1.20 ± 0.60 Gyr	[Bonfanti 15]
Magnetic Field Strength	3.2 ± 0.3 G	[Cauley 19]
Stellar Rotational Period	Equatorial: 7.62 ± 0.05 days Polar : 10.30 ± 0.80 days	[Fares 12]
Planet Orbit Radius	0.044 ± 0.003 AU	[Butler 06]
Orbit Inclination	67.7 ± 4.3°	[Butler 06]
Planet Orbital Period	3.09285 ± 0.00056 days	[Shkolnik 04]
Planet Conjunction Epoch (JD - 2,400,000)	52479.823 ± 0.093 days	[Shkolnik 04]
Planet Mass	0.98 ± 0.004 $M_{Jupiter}$	[Butler 06]
Planet Radius	1.05 $R_{Jupiter}$	[Wang 11]

^aCompiled resources from the various catalogues cited can be found at SIMBAD: Set of Identifications, Measurements and Bibliography for Astronomical Data. Website: <http://simbad.u-strasbg.fr/simbad/>

Chapter 2

Observations

Given that our primary aim was to observe the corona of HD179949 which is a Sun-like star, the expected temperatures for the same are $> 10^6 K$, which implies that the majority of the emission shall be in the EUV and soft X-ray regime. For observing in the soft X-ray regime, the Advanced CCD Imaging Spectrometer (ACIS) of the Chandra X-ray Observatory has been used, given that it operates within the range of 0.2 - 10 keV, and provides images as well as spectral information of the objects observed.

A thorough understanding of handling and using X-ray data can be achieved by going through the X-ray Data Primer provided by the Chandra X-ray Centre ([Lee 11]).

2.1 Chandra X-ray Observatory

The Chandra X-ray Observatory¹ is the third of the Great Observatories launched by NASA, which includes the Hubble Space Telescope, the Compton Gamma Ray Observatory (de-orbited in 2000), the Chandra X-ray Observatory, and the Spitzer Space Telescope (placed in safe mode since January 2020). It has 4 scientific instruments, two of which are focal plane instruments.

One is the High Resolution Camera (HRC), which is used for high resolution imaging, fast timing measurements, and for observations requiring a combination of both. The second is the ACIS, which contains 10 planar, 1024×1024 pixel CCDs; four arranged in a 2×2 array (ACIS-I) used for imaging, and six arranged in a 1×6 array (ACIS-S) used either for imaging or for a grating spectrum read-out. Two CCDs are back-illuminated (BI) and eight are front-illuminated (FI). The ACIS has a point-source sensitivity of 4×10^{-15} ergs $cm^{-2}s^{-1}$ in 10^4 s in the 0.4 - 6.0 keV regime. While spatial resolution is limited by the physical size of the CCD pixels ($24.0 \mu m$ square, ~ 0.492 arcsec), approximately 90% of

the encircled energy lies within 4 pixels (2 arcsec) of the center pixel at 1.49 keV and within 5 pixels (2.5 arcsec) at 6.4 keV. The ACIS energy resolution (the full width at half maximum [FWHM] of a narrow spectral line) varies roughly as the square root of the energy, and increases with distance from the read-out. It is ~ 0.095 keV at 1.49 keV, and ~ 0.150 keV for the S3 (CCD ID 7) chip, which is the best for imaging and also has the S-array aimpoint.

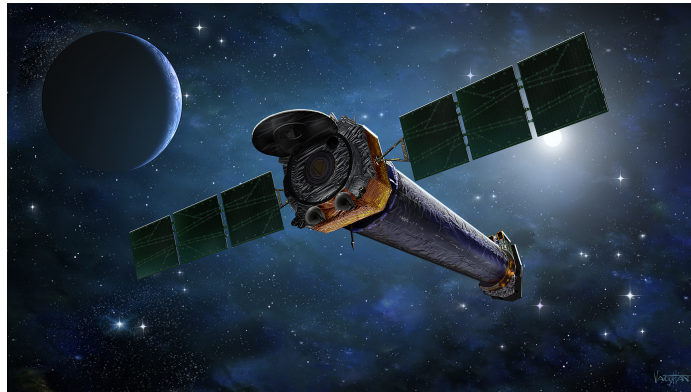


Figure 2.1: The Chandra X-ray Observatory is the world's most powerful X-ray telescope. It has eight-times greater resolution and is able to detect sources more than 20-times fainter than any previous X-ray telescope. *Credits: NASA/CXC & J.Vaughan*

ACIS and HRC can be used in conjunction with one of the observatory's two transmission gratings. The transmission gratings, which swing into the optical path behind the mirrors, provide Chandra with high resolution spectroscopy. The High Energy Transmission Grating Spectrometer (HETGS) works over 0.4–10 keV and has a spectral resolution of 60–1000. The Low Energy Transmission Grating Spectrometer (LETGS) has a range of 0.09–3 keV and a resolution of 40–2000.

2.2 Data Used

The data sets used for this project have observation IDs 5427, 6119, 6120, 6121, and 6122, from the archives of the Chandra X-ray Observatory. The PI for these observations is **Dr. Steven Saar**. The observations were taken in May 2005 with the observation IDs 5427, 6119, 6120 and 6121 having an exposure time of ~ 29.6 ksec, and observation ID 6122 has an exposure time of ~ 31.8 ksec. A slight offset is noted from the expected Right Ascension and Declination of the star, on calculating the centroid of the incoming photons from the source for each data set. In Figure 2.2, the expected position of the star, and the

¹More information about the Chandra X-ray Observatory can be found at: https://cxc.harvard.edu/cdo/about_chandra/overview_cxo.html

Table 2.1. Observation Log:

ObsID	Observation Date & Time	Exposure Time [ksec]	Planetary phase range ^a [deg]
5427	2005-05-21 18:12:41	29.581	292.945 - 332.795 ± 24.303
6119	2005-05-22 11:37:35	29.648	17.490 - 57.431 ± 24.316
6120	2005-05-29 16:51:03	29.648	137.526 - 177.467 ± 24.453
6121	2005-05-30 12:00:30	29.644	203.933 - 243.870 ± 24.464
6122	2005-05-31 10:50:19	31.763	318.626 - (360+)1.416 ± 24.482

^aPhase = 0 is for the planet being in front of the star, i.e., between the star and the observer. The ephemeris for $\phi=0$ is taken from [Shkolnik 04] and is 2452479.823 ± 0.093 days.

position at the J2000 epoch and equinox is shown. Tables 2.1 and 2.2 summarise the details of the observations.

The data are analysed using the CIAO (Chandra Interactive Analysis of Observations)² software. CIAO is a free software package developed by the Chandra X-ray Centre, for analysing data from the Chandra X-ray telescope. However, it can also be used with other ground and space-based observatories ([Fruscione 06]).

The image observed in the SKY coordinates and in CHIP coordinates with CCD ID = 7 are shown in Figure 2.3. The SKY coordinate system is measured in pixels in the tangent plane. These pixel numbers can be converted to celestial Right Ascension and Declination using programs like *dmcoords* or softwares like DS9³. For Chandra data, the X and Y axes are aligned with J2000 RA and Dec in the ICRS (Hipparcos) frame. The CHIP coordinate system gives row and column number on each chip. This is the most-basic coordinate system in the event file. The numbering starts at (1,1) in the lower left corner of the chip and starts over on each chip. For ACIS, the chips are 1024 x 1024 pixels in size and each chip has a number (CCD ID) from 0 to 9. Note that the chip X axes are not all pointing in the same direction in the spacecraft. In the event files, the CHIP values are integers.

²For more information on the software, check: <https://cxc.cfa.harvard.edu/ciao/>.

³SAOImage DS9 is an astronomical imaging and data visualization application. DS9 supports FITS images and binary tables, multiple frame buffers, region manipulation, and many scale algorithms and colormaps.

Table 2.2. Summary of Chandra observations

ObsID	Measured Position	Offset from expected position	Counts in source region ^a	Counts in background region ^b	Net Counts ^a	Net Rate ^a [ct ksec ⁻¹]
5427	19:15:33.2990 ± 0.405", -24° 10' 46.127"	+0.520", -0.011"	1597	124	1594.7 ±41.0	53.9 ±1.4
6119	19:15:33.2853 ± 0.351", ± 0.300", -24° 10' 46.159"	+0.305", -0.044"	1300	118	1297.9 ±37.1	43.9 ±1.3
6120	19:15:33.2849 ± 0.311", ± 0.435", -24° 10' 46.084"	+0.299", +0.033"	1458	117	1455.87 ±39.2	49.1 ±1.3
6121	19:15:33.2850 ± 0.405", -24° 10' 46.061"	+0.304", +0.056"	1599	116	1596.89 ±41.0	53.9 ±1.4
6122	19:15:33.2887 ± 0.390", -24° 10' 46.049"	+0.358", +0.069"	1934	497	1924.96 ±45.0	60.6 ±1.4

^ain broad band 0.5-7.0 keV.

^bbackground scaling factor = 1/55.

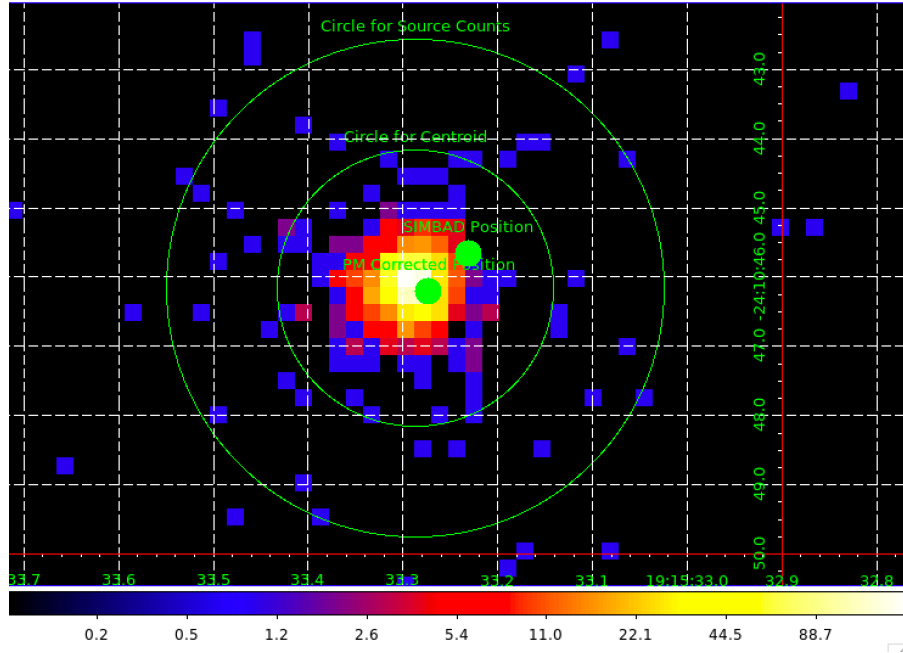


Figure 2.2: Image of HD179949 with the “PM corrected position” marker showing the measured position after taking proper motion into account, while the “SIMBAD position” marker shows the expected position from SIMBAD. The inner circle marked as the “Circle for Centroid” has a 2” radius and is used for centroiding. The outer circle marked as “Circle for Source Counts” has a 3.6” radius and is used to get the total number of counts from the source.

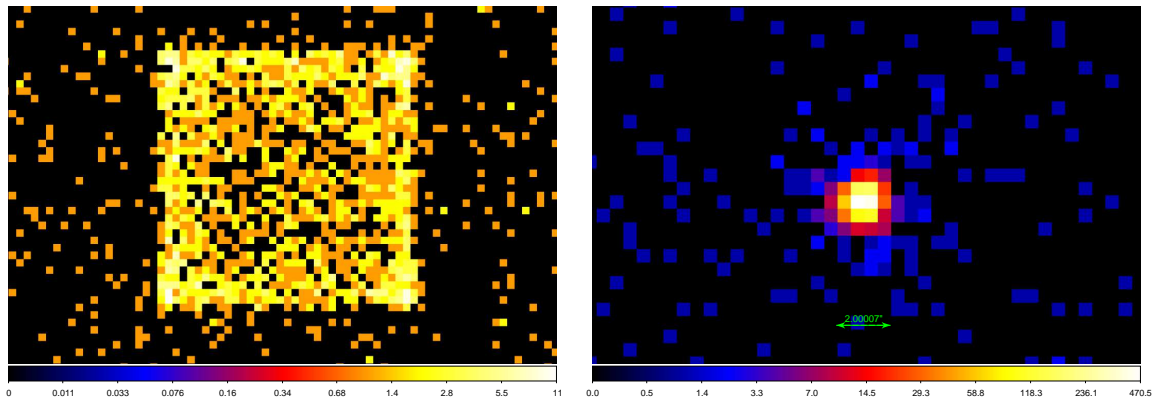


Figure 2.3: Left: Image in CHIP coordinates with CCD ID = 7 and Right: Image in SKY coordinates

Chapter 3

Analysis

The FITS file of each data set (say 6119) is opened in SAOImage DS9³ to extract the source and background regions. For this, firstly the centroid of the photon counts is identified. This is used as the centre for a circle of radius 3.6 arcseconds (shown in Figure 2.2), which is defined as the “source circle”. It is assumed that there is no spillage of source photons beyond this “source circle”, i.e., all counts from the source, are assumed to come from this region. This assumption is verified by calculating the average counts-weighted Point Spread Function fraction, which is $> 95\%$ for all data sets for the source circle radius chosen.

The centroid is also used as a centre for an annulus with inner and outer radii 10.8 arcseconds and 28.8 arcseconds respectively. All counts from this region are taken to be coming from the background. The details of the measured number of counts from these regions is listed in Table 2.2.

3.1 Spectral Fits

Using the above mentioned source and background regions, the spectrum of the source was obtained using the *specextract* script on CIAO. The *specextract* script runs the following steps:

- *dmextract* : to extract the source and if necessary, also the background spectra. This tool also creates the WMAP (Weight Map, which is a 2D image binned in detector coordinates) used as input to *mkacisrmf*.
- *mkarf* : to create ARFs (Auxiliary Response Files).
- *arfcorr* : to apply an energy-dependent point-source aperture correction to the source ARF file.

- *mkrmf* or *mkacisrmf* : to build the RMFs (Redistribution Matrix Files), depending on which is appropriate for the data and the calibration.
- *dmgroup* : to group the source spectrum and/or background spectrum.
- *dmhedit* : to update the BACKFILE (the keyword for the PHA i.e., Pulse Height Amplitude file containing the background for the source), RESPFILE (the keyword for the RMF file for the source) and ANCRFILE (the keyword for the ARF file for the source) keys in the source and background spectrum files

As the star is a point source, there was no necessity for the responses to be weighted by the count distribution within the aperture, so the *weight* parameter was set as “no”. However, the *correctpsf* parameter was set as “yes” so that the ARF is corrected for events falling outside the finite size and shape of the aperture. Running the *specextract* script gave us 4 files, a .arf file, a .rmf file, a .corr.arf file (the corrected version of the .arf file generated as *correctpsf* was set to “yes”) and a .pi file.

The .arf file includes information about the effective area, filter transmission and any additional energy-dependent efficiencies, thus giving us an idea about how sensitive the instrument is in detecting photons. The .rmf file describes the probability that a photon of a given energy is registered with a particular detector signal strength. For X-ray spectral analysis, the RMF encodes the probability $R(E,p)$ that a detected photon of energy E will be assigned to a given channel value (PHA or PI) of p . Lastly, the .pi file has the information for the spectrum of the source.

For this spectrum, a series of attempts were carried out to zero in on a model that reasonably explains the observations. For all models, the multiplicative XSPEC ([Arnaud 96]) Tübingen-Boulder absorption model was used for ISM absorption, referred to as **xstbabs**. Note that the hydrogen column density variable in this model, N_H was fixed at 10^{19} cm^{-2} for all models as done in [Scandariato 13]. For emission spectra, **xsvapec** was used for all models discussed below, which is an APEC ([Brickhouse 00],[Smith 01]) emission spectrum from collisionally-ionized diffuse plasma calculated from the AtomDB⁴ atomic database ([Foster 16]). It is an additive model component, which allows the varying of the plasma temperature, abundances for He, C, N, O, Ne, Mg, Al, Si, S, Ar, Ca, Fe and Ni, the redshift and the norm. The AtomDB line and continuum results apply to any optically-thin thermal plasma with astronomical abundances (like [Anders 89]). Calculating the X-ray spectrum of any hot, collisionally-dominated optically-thin plasma requires us to know the atomic transition rates and energies of the ions involved, as well as being able to calculate how the

different rates affect each other. For doing this, the AtomDB database keeps the following relevant processes in mind:

- Continuum emission processes
 1. Free-bound emission (radiative recombination)
 2. 2-photon emission
- Line emission process
 1. One-electron radiative transitions
 2. Dielectronic recombination satellite lines
 3. Inner-shell ionization

The AtomDB database does not consider some processes like *two-photon excitation* (and other three-body processes as they need densities beyond the ‘optically-thin’ limit. *Charge exchange processes* are omitted because these processes usually arise from the interaction of hot ions and neutral H or He. But in hot plasmas at or near equilibrium, neutral H and He are not present in significant volumes. And lastly, as we consider a collisionally-dominated plasma, AtomDB also ignores photoionisation. Given that we are dealing with the coronal region, our plasma emission models operate in the low density regime, that is, we took the approximation of ignoring collisional de-excitation, so every excited level was assumed to decay via a radiative transition.

Lastly, the abundance values are scaled with respect to the solar photospheric abundances listed in [Anders 89]. While there are other solar abundances that can be used, we chose this as it is the most widely used.

For evaluating the models generated, we calculated the goodness of fit for C-statistic. It is to be noted that χ^2 test cannot be performed for low counts Poisson data, for evaluating the goodness of a fit, as detailed in [Kaastra 17]. To check the goodness of fit, the observed C-statistic of the fit is compared with the expected C-statistic. If the expected C-statistic is more than 2 standard deviations away from the observed value, we rejected the model as it was unlikely to be a good fit. It must be noted that there can be multiple models with the $|\text{Expected} - \text{Observed}|$ value of the C-statistic being $< 2\sigma$, in which case the nature of the residuals was evaluated. In particular, a good fitting model is expected to not have residuals that strongly correlate to specific spectral line regions, and if that occurs, it can

⁴More information about the database can be found on their website at <http://www.atomdb.org>

be taken as an indication of more complex models being needed. For a good fitting model, any residuals observed are expected to be random deviations from the expected values.

A good way to quantify the behaviour of residuals is to perform the Cumulative Sum (CUSUM) test. The CUSUM test is a sequential analysis test developed to monitor change detection. For the test, once the parameters of a spectral fit are ascertained, we calculate the cumulative sum of residuals with increase in energy. It is to be noted that the sign of the residual matters as well, to keep track of the regions where the fit over/under-predicts as compared to the actual data. Next, we use the *fake_pha* command to simulate a large distribution of 1-D PHA (Pulse Height Amplitude) data. The cumulative sum of residuals are calculated for each of these distributions, and we find the 5th and 95th percentile cumulative sum trends of this distribution. If the cumulative sum trend of the actual data falls in between these, we can conclude that we have gotten a good fit. If not, we shall be able to see the energy ranges where the fit does not work.

- **Model A :** The first model assumed the simplest condition of a single temperature for the entire coronal region, and one metallicity for all metals. This was done to understand how much deviation can be observed in the spectra from the most basic attributes.

The fit obtained by this model showcases a host of issues for all the data sets. Across all data sets, the residuals are found to strongly correlate with energy regions, indicating that some metals were being consistently under-predicted, while the others were being over-predicted. Such strongly correlated residuals are a clear indication of more complex features being necessary.

Further, the goodness of fit calculation using the Cash-statistic shows a $> 2.5\sigma$ deviation, thus showing that this is not a good fit. We also perform the CUSUM test, and find $> 45\%$ of bins to be beyond the 5th to 95th percentile range, with the maximum cumulative sum going > 0.1 , thus strengthening the need for a better fit.

- **Model B :** The next step to improve on this model was to assume a 2 temperature system, rather than a homogeneous single temperature coronal structure. This allows for some of the variations observed to be assigned to the hotter component, and some to a cooler component.

We still allow the metallicity to vary as a whole, rather than setting individual abundances, to understand the role of the 2 temperature component. This leads to some improvement and the goodness of fit calculation gives a low deviation of just $< 0.30\sigma$ for observation IDs 5427 and 6119. However, for observation IDs 6120, 6121 and 6122, the Cash statistic still shows $> 1.8\sigma$ deviation.

Further, the residuals still remained strongly correlated and their magnitude is in fact worse for the 0.5-0.9 keV regime. The same can be noted in the CUSUM test, where while very low number of bins ($< 15\%$) go beyond the 5th to 95th percentile regime, the maximum deviations are very high (> 0.075).

Clearly, changing individual abundances of metals would be necessary to improve the spectral fitting across all data sets.

- **Model C :** An improvement on the 2-temperature model can be made by setting individual abundances of metals. For this model, we work with the assumption that the chromospheric metallicities noted by [Scandariato 13] hold true for the coronal regions as well.

For this, we set iron abundance as 0.5 Fe_\odot , $\text{O/Fe} = 0.3$, $\text{Ne/Fe} = 0.5$, $\text{Si/Fe} = 0.9$ and all other metals are tied to iron. While there is no marked difference in the residuals, the goodness of fit measured by the Cash statistic is found to be $> 3.5\sigma$ for all data sets. Even the CUSUM test shows $> 50\%$ bins deviating from the 5th to 95th percentile regime with the maximum cumulative sum > 0.1 for all data sets. Clearly, the chromospheric abundances do not reflect the coronal abundances. However the first two models showcase that one value for abundance of all metals does not capture the picture either. Hence we try another model.

- **Model D :** In this, a 2-temperature **xsvapec** model is assumed with the abundances of various metals being allowed to vary. Some metals are tied together, for example, Carbon and Oxygen are tied together, and so are Nickel and Iron. Further, Sulphur, Argon and Calcium are tied together as well.

The resultant fits give us a goodness of fit measure of $\sim 1\sigma$ for all data sets, and even for the CUSUM test, $< 5\%$ of the bins go beyond the 5th to 95th percentile regime. Further, the maximum values of the cumulative sum are $\sim < 0.05$, which indicates that the spectral fitting model obtained can be assumed to be a good estimate of the observations.

We find that the model predicts high abundances for Al, Ca and N as compared to their solar abundances. Fe is found to be around 0.4 Fe_\odot on an average for all data sets, while O is around 0.27 O_\odot .

The details of all 4 models are given in tables 3.1, 3.2, 3.3 and 3.4. The 4 models for observation IDs 6120 and 6121 are shown in Figs. 3.2 and 3.3 respectively, with the two components of Models B, C and D plotted as well. Note that the component with the higher peak in each case represents the hotter component. Further, in the graphs, the residuals are

Table 3.1. Spectral Fits for Model A:

Parameters \ ObsID	5427	6119	6120	6121	6122
T [MK]	$6.23^{+0.20}_{-0.21}$	$5.44^{+0.40}_{-0.35}$	$5.49^{+0.39}_{-0.34}$	$6.25^{+0.44}_{-0.40}$	$6.62^{+0.29}_{-0.26}$
Z	$0.14^{+0.02}_{-0.02} Z_{\odot}$	$0.16^{+0.06}_{-0.04} Z_{\odot}$	$0.14^{+0.04}_{-0.03} Z_{\odot}$	$0.15^{+0.04}_{-0.03} Z_{\odot}$	$0.14^{+0.04}_{-0.03} Z_{\odot}$
norm [10^{-4} cm^{-5}]	$3.35^{+0.27}_{-0.26}$	$2.87^{+0.60}_{-0.55}$	$3.50^{+0.64}_{-0.59}$	$3.23^{+0.56}_{-0.57}$	$3.58^{+0.55}_{-0.51}$
Goodness of Fit	$+2.55\sigma$	$+1.23\sigma$	$+2.54\sigma$	$+2.40\sigma$	$+3.34\sigma$
Max. Cusum	0.12	0.15	0.11	0.10	0.10
Flux (0.15 - 4.0 keV) [$10^{-13} \text{ erg s}^{-1} \text{ cm}^{-2}$]	$2.37^{+0.24}_{-0.28}$	$2.12^{+0.22}_{-0.19}$	$2.32^{+0.27}_{-0.29}$	$2.44^{+0.24}_{-0.29}$	$2.73^{+0.28}_{-0.21}$
No. of bins beyond 5th-95th percentile	149/453	40/453	37/453	223/453	245/453

Table 3.2. Spectral Fits for Model B:

Parameters \ ObsID	5427	6119	6120	6121	6122
T1 [MK]	$6.47^{+0.36}_{-0.46}$	$6.13^{+0.47}_{-0.57}$	$5.82^{+0.52}_{-0.46}$	$6.70^{+0.63}_{-0.86}$	$6.86^{+0.37}_{-0.37}$
T2 [MK]	$1.06^{+0.96}_{-0.56}$	$1.33^{+1.17}_{-0.46}$	$1.01^{+0.95}_{-0.58}$	$2.45^{+1.24}_{-0.74}$	$2.37^{+1.34}_{-1.34}$
Z	$0.23^{+0.13}_{-0.08} Z_{\odot}$	$0.34^{+0.39}_{-0.14} Z_{\odot}$	$0.21^{+0.14}_{-0.07} Z_{\odot}$	$0.21^{+0.11}_{-0.06} Z_{\odot}$	$0.19^{+0.08}_{-0.09} Z_{\odot}$
norm1 [10^{-4} cm^{-5}]	$2.28^{+1.21}_{-0.74}$	$1.36^{+0.84}_{-0.68}$	$2.41^{+1.06}_{-0.88}$	$2.25^{+0.83}_{-0.70}$	$2.78^{+1.53}_{-0.75}$
norm2 [10^{-4} cm^{-5}]	$3.26^{+5.78}_{-3.07}$	$1.56^{+6.08}_{-1.05}$	$5.03^{+0.59}_{-0.47}$	$0.57^{+0.70}_{-0.38}$	$0.54^{+0.45}_{-0.36}$
Goodness of Fit	$+0.25\sigma$	$+0.30\sigma$	$+2.18\sigma$	$+1.82\sigma$	$+3.06\sigma$
Max. Cusum	0.06	0.07	0.09	0.06	0.08
Flux (0.15 - 4.0 keV) [$10^{-13} \text{ erg s}^{-1} \text{ cm}^{-2}$]	$2.38^{+0.58}_{-0.40}$	$2.16^{+0.52}_{-0.49}$	$2.52^{+0.67}_{-0.69}$	$2.45^{+0.62}_{-0.40}$	$2.73^{+0.43}_{-0.38}$
No. of bins beyond 5th-95th percentile	58/453	49/453	38/453	179/453	242/453

Table 3.3. Spectral Fits for Model C:

Parameters \ ObsID	5427	6119	6120	6121	6122
T1 [MK]	$6.84^{+0.69}_{-0.36}$	$6.67^{+0.98}_{-0.66}$	$6.02^{+0.57}_{-0.44}$	$7.23^{+0.60}_{-0.56}$	$7.38^{+33.81}_{-0.50}$
T2 [MK]	$2.03^{+0.75}_{-0.65}$	$2.33^{+0.60}_{-0.56}$	$1.77^{+0.57}_{-0.44}$	$2.50^{+0.34}_{-0.61}$	$2.49^{+0.44}_{-0.59}$
norm1 [10^{-4} cm^{-5}]	$1.17^{+0.12}_{-0.28}$	$0.84^{+0.20}_{-0.28}$	$1.19^{+0.18}_{-0.21}$	$1.02^{+0.20}_{-0.18}$	$1.16^{+0.20}_{-0.90}$
norm2 [10^{-4} cm^{-5}]	$1.36^{+1.37}_{-0.31}$	$1.43^{+0.32}_{-0.30}$	$1.68^{+1.40}_{-0.57}$	$1.29^{+0.33}_{-0.30}$	$1.34^{+0.32}_{-0.30}$
Goodness of Fit	$+1.37\sigma$	-0.15σ	$+3.35\sigma$	$+3.67\sigma$	$+5.95\sigma$
Max. Cusum	0.12	0.11	0.12	0.11	0.17
Flux (0.15 - 4.0 keV) [$10^{-13} \text{ erg s}^{-1} \text{ cm}^{-2}$]	$2.63^{+0.21}_{-0.30}$	$2.24^{+0.24}_{-0.22}$	$2.52^{+0.23}_{-0.26}$	$2.57^{+0.14}_{-0.15}$	$2.85^{+0.14}_{-0.15}$
No. of bins beyond 5th-95th percentile	237/453	101/453	96/453	253/453	266/453

not large and are $\lesssim \Delta\chi = 2$ for all fits. Figs. 3.4 and 3.5 show the variation of the cumulative sum versus energy for the 4 models for the observation IDs 6120 and 6121 respectively.

It is to be noted that after obtaining the fits for Model D, we performed Bayesian Low-Count X-ray Spectral (BLoCXS) analysis using the pyBLoCXS package ([Kashyap 98],[van Dyk 01]) in the Sherpa environment by calling the *get_draws()* function. This is a sophisticated Markov Chain Monte Carlo (MCMC) method ([Speagle 20], [Neal 93]) that explores parameter space at a suspected minimum using a predefined Sherpa model to high-energy X-ray spectral data. The results obtained from this are reported in table 3.4. The corner plot for observation ID 6120 showcasing the results for the MCMC draws for all parameters is showcased in Fig. 3.1.

Table 3.4. Spectral Fits for Model D:

Parameters \ ObsID	5427	6119	6120	6121	6122
T1 [MK]	$8.24^{+1.51}_{-1.28}$	$6.71^{+0.41}_{-0.39}$	$9.13^{+2.91}_{-4.12}$	$8.12^{+0.35}_{-0.23}$	$10.10^{+0.70}_{-1.04}$
T2 [MK]	$4.87^{+0.70}_{-0.93}$	$3.45^{+1.14}_{-0.98}$	$4.96^{+0.28}_{-0.37}$	$6.03^{+0.46}_{-0.23}$	$4.64^{+0.46}_{-0.70}$
N	$4.64^{+2.39}_{-1.72} \text{ N}_{\odot}$	$3.16^{+2.10}_{-1.64} \text{ N}_{\odot}$	$2.82^{+2.47}_{-1.84} \text{ N}_{\odot}$	$3.76^{+0.99}_{-0.96} \text{ N}_{\odot}$	$0.60^{+0.75}_{-0.44} \text{ N}_{\odot}$
O	$0.24^{+0.14}_{-0.13} \text{ O}_{\odot}$	$0.30^{+0.14}_{-0.06} \text{ O}_{\odot}$	$0.24^{+0.20}_{-0.09} \text{ O}_{\odot}$	$0.60^{+0.10}_{-0.07} \text{ O}_{\odot}$	$0.24^{+0.09}_{-0.05} \text{ O}_{\odot}$
Ne	$0.19^{+0.06}_{-0.11} \text{ Ne}_{\odot}$	$0.05^{+0.06}_{-0.03} \text{ Ne}_{\odot}$	$0.23^{+0.17}_{-0.10} \text{ Ne}_{\odot}$	$0.06^{+0.18}_{-0.05} \text{ Ne}_{\odot}$	$0.03^{+0.03}_{-0.03} \text{ Ne}_{\odot}$
Mg	$0.60^{+0.19}_{-0.17} \text{ Mg}_{\odot}$	$0.53^{+0.15}_{-0.19} \text{ Mg}_{\odot}$	$0.88^{+0.24}_{-0.21} \text{ Mg}_{\odot}$	$0.21^{+0.10}_{-0.06} \text{ Mg}_{\odot}$	$0.55^{+0.24}_{-0.17} \text{ Mg}_{\odot}$
Al	$3.09^{+2.91}_{-1.09} \text{ Al}_{\odot}$	$3.87^{+4.70}_{-0.96} \text{ Al}_{\odot}$	$4.56^{+3.76}_{-2.50} \text{ Al}_{\odot}$	$1.08^{+1.41}_{-0.48} \text{ Al}_{\odot}$	$2.86^{+1.03}_{-1.08} \text{ Al}_{\odot}$
Si	$1.02^{+0.45}_{-0.45} \text{ Si}_{\odot}$	$0.46^{+0.33}_{-0.20} \text{ Si}_{\odot}$	$0.82^{+0.26}_{-0.26} \text{ Si}_{\odot}$	$0.23^{+0.04}_{-0.13} \text{ Si}_{\odot}$	$0.49^{+0.17}_{-0.13} \text{ Si}_{\odot}$
Ca	$1.06^{+0.44}_{-0.65} \text{ Ca}_{\odot}$	$1.03^{+0.59}_{-0.65} \text{ Ca}_{\odot}$	$1.24^{+1.41}_{-0.78} \text{ Ca}_{\odot}$	$0.19^{+0.22}_{-0.16} \text{ Ca}_{\odot}$	$0.23^{+0.26}_{-0.16} \text{ Ca}_{\odot}$
Fe	$0.45^{+0.09}_{-0.11} \text{ Fe}_{\odot}$	$0.44^{+0.06}_{-0.08} \text{ Fe}_{\odot}$	$0.44^{+0.14}_{-0.09} \text{ Fe}_{\odot}$	$0.28^{+0.02}_{-0.03} \text{ Fe}_{\odot}$	$0.31^{+0.06}_{-0.05} \text{ Fe}_{\odot}$
norm1 [10^{-4} cm^{-5}]	$0.49^{+0.44}_{-0.24}$	$0.88^{+0.11}_{-0.33}$	$0.12^{+0.11}_{-0.06}$	$0.62^{+0.18}_{-0.14}$	$0.72^{+0.17}_{-0.17}$
norm2 [10^{-4} cm^{-5}]	$1.07^{+0.41}_{-0.44}$	$0.65^{+0.29}_{-0.22}$	$1.34^{+0.37}_{-0.23}$	$1.20^{+0.22}_{-0.09}$	$1.90^{+0.28}_{-0.28}$
Goodness of Fit	-0.82σ	-1.18σ	$+0.92\sigma$	$+1.20\sigma$	-1.46σ
Max. Cusum	0.03	0.04	0.07	0.05	0.05
Flux (0.15 - 4.0 keV) [$10^{-13} \text{ erg s}^{-1} \text{ cm}^{-2}$]	$2.43^{+0.09}_{-0.07}$	$2.08^{+0.09}_{-0.06}$	$2.38^{+0.05}_{-0.08}$	$2.39^{+0.05}_{-0.07}$	$2.74^{+0.03}_{-0.08}$
No. of bins beyond 5th-95th percentile	21/453	18/453	13/453	14/453	18/453

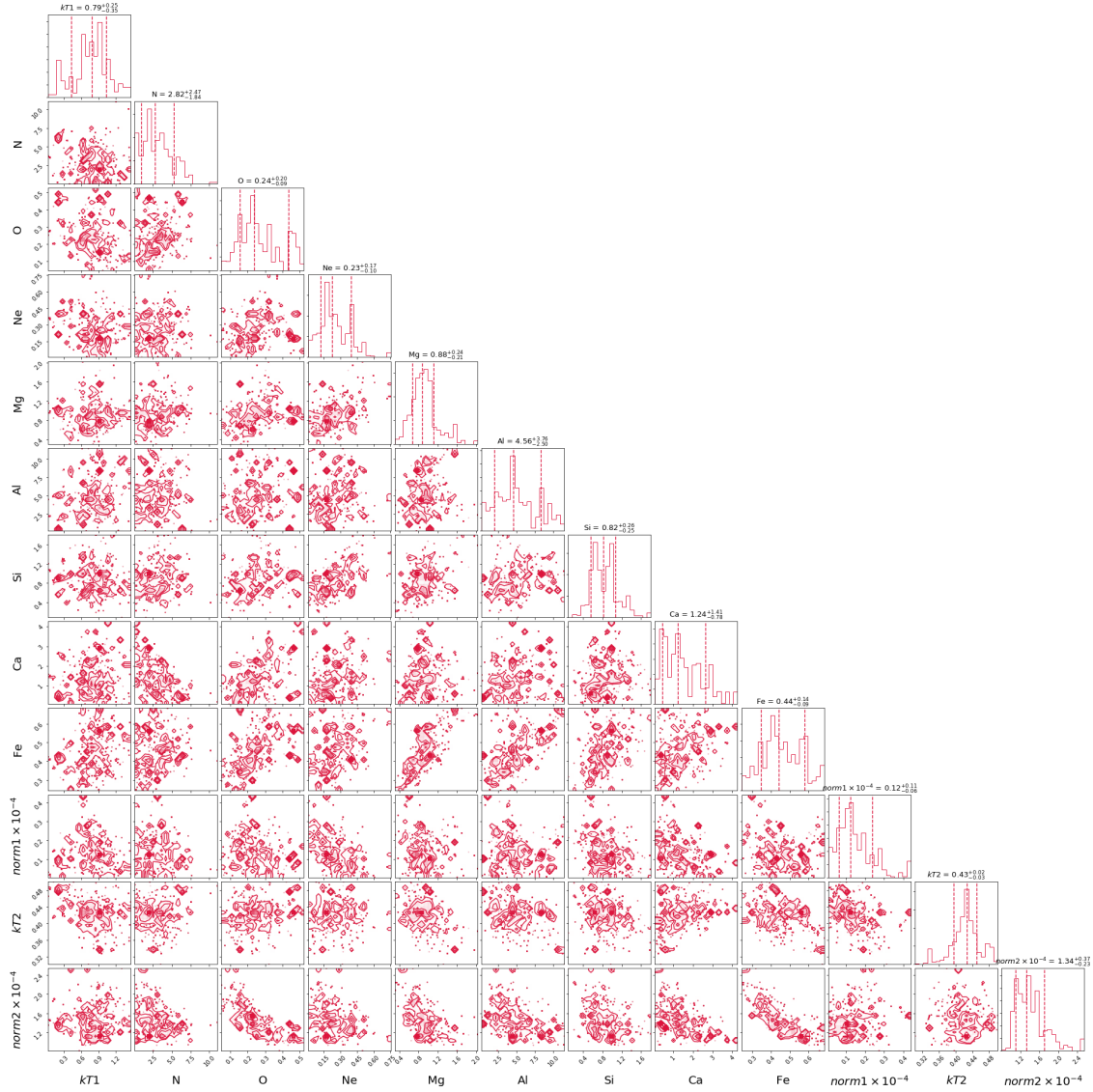


Figure 3.1: Corner Plot showcasing results from MCMC draws using the pyBLoCXS package for observation ID 6120. The error bars are showcased by the 16th to 84th percentile range dashed lines (left and right most for each parameter) and the accepted value is the 50th percentile value given by the central dashed line.

Based on the resultant norms and temperatures of the 2 components of the stellar corona for model D, we calculated the fractional volume covered by each component, and the scale height of the region. The volume of each component is calculated by:

$$norm = \frac{V \times n^2}{4\pi D^2} \quad (3.1)$$

where D is the distance of the star from the observer, which in our case is 27.4789 pc. Also, n is the number density of plasma particles (electrons and protons). Now, the smallest possible X-ray feature observable on the Sun would be 1'' on the side as observed from Earth, which is approximately 700 km ([Glesener 17]). Thus, we can assume that the smallest

possible X-ray feature on the star HD179949 shall have a fractional coverage of $f_{min} = (700 \text{ km})^2 / S.A._{HD179949}$, where $S.A._{HD179949}$ is the total surface area of the star. This gives us $f_{min} = 5.58 \times 10^{-6}\%$. This can be used to find the upper limit of the range of plasma densities. For the lower limit, we can assume 100 % coverage. Now, from the values of the norms for the 2 temperature model we get a range of $\log(n_{plasma}) \sim 9.1$ and $\log(n_{plasma}) \sim 12.4$. This is in agreement with what is known about Sun-like stars, for whom the $\log(n_{plasma})$ ranges from 9 to 10. Taking both of the above points into account, we assume $n_{plasma} = n_{electrons} = 5 \times 10^9 \text{ cm}^{-3}$.

Next, the scale height is given by:

$$H = \frac{kT}{m_H g} \quad (3.2)$$

where m_H is the mass of the Hydrogen atom, as we assume that all particles in the corona are Hydrogen atoms.

Which finally gives us the fractional surface area covered by each component as:

$$f(in\%) = 100 \times \frac{V}{H \times S.A._{star}} \quad (3.3)$$

Where V is the volume calculated earlier, and H is the scale height. $S.A._{star}$ is the total surface area of the star, which was trivially calculated as $S.A._{star} = 4\pi R_{star}^2$, where R_{star} is the mean stellar radius, which is $1.20R_{\odot}$ for HD179949. The results of these calculations are shown in Table 3.5. From Table 3.5 we get the range of scale heights for the hotter component to be from 2.42 to $3.64 \times 10^{10} \text{ cm}$, while that for the cooler component varies between 1.24 to $2.16 \times 10^{10} \text{ cm}$. These results are fairly comparable to the coronal scale heights of the Sun, which are found to be of the order of 10^{10} cm .

Table 3.5. Derived properties of the Stellar Corona:

Parameters \ ObsID	5427	6119	6120	6121	6122
Hotter Component					
Volume [$\times 10^{33} \text{ cm}^{-3}$]	2.62	2.12	2.89	2.56	3.20
Scale Height [$\times 10^{10} \text{ cm}$]	2.98	2.42	3.29	2.92	3.64
Fractional Surface Area [%]	4.94	6.09	4.47	5.05	4.04
Cooler Component					
Volume [$\times 10^{33} \text{ cm}^{-3}$]	1.53	1.09	1.57	1.89	1.47
Scale Height [$\times 10^{10} \text{ cm}$]	1.75	1.24	1.79	2.16	1.67
Fractional Surface Area [%]	8.43	11.85	8.25	6.82	8.79

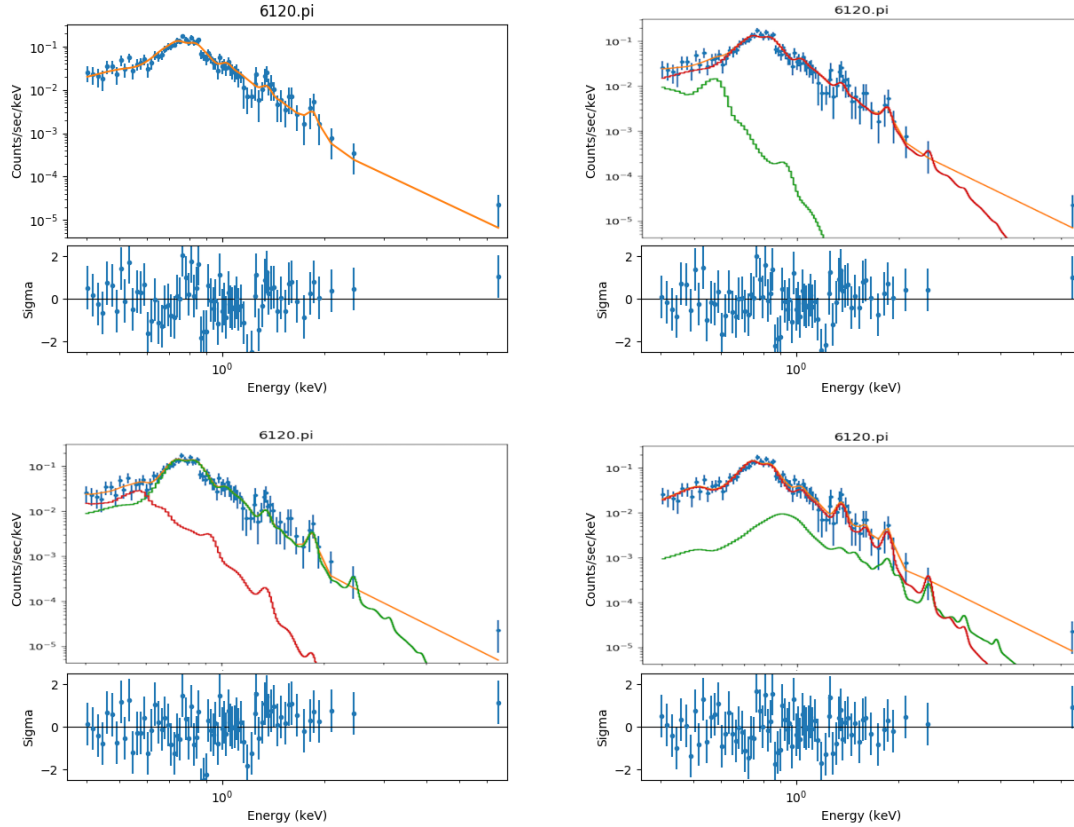


Figure 3.2: For observation ID 6120: **Top Left:** Spectral fit for Model A; **Top Right:** Spectral fit for Model B. **Bottom Left:** Spectral fit for Model C. **Bottom Right:** Spectral fit for Model D.

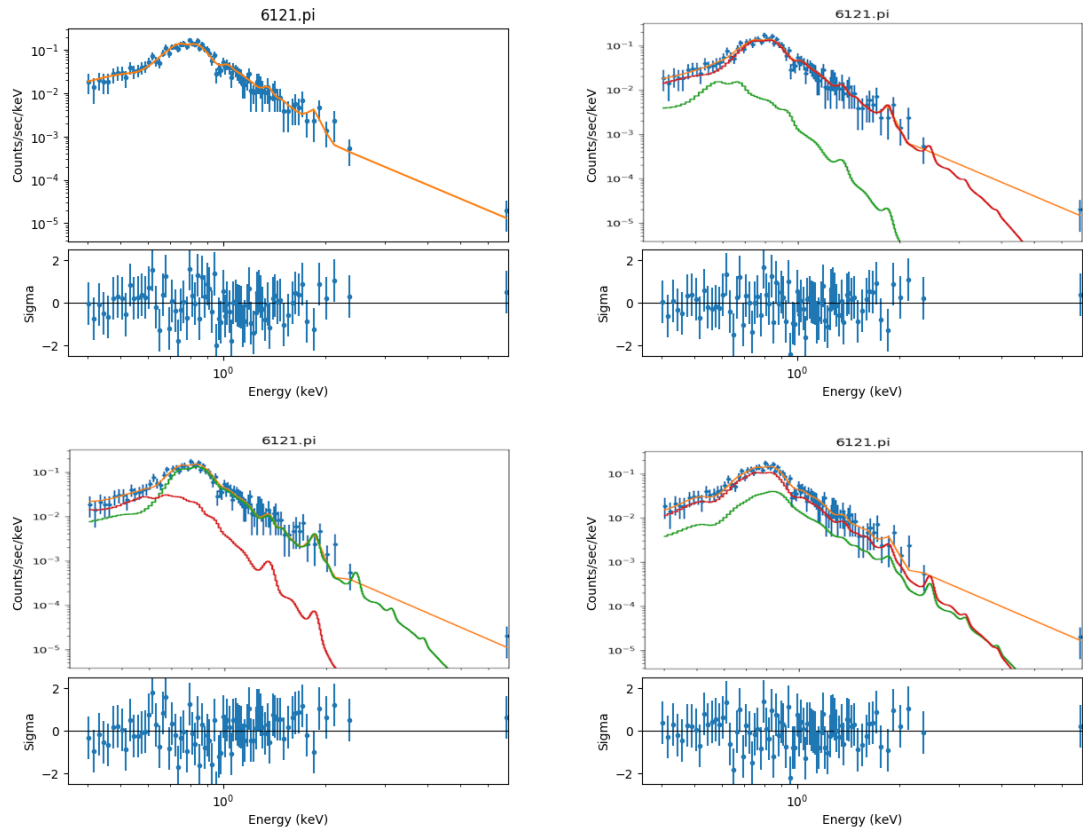


Figure 3.3: For observation ID 6121: **Top Left:** Spectral fit for Model A; **Top Right:** Spectral fit for Model B. **Bottom Left:** Spectral fit for Model C. **Bottom Right:** Spectral fit for Model D.

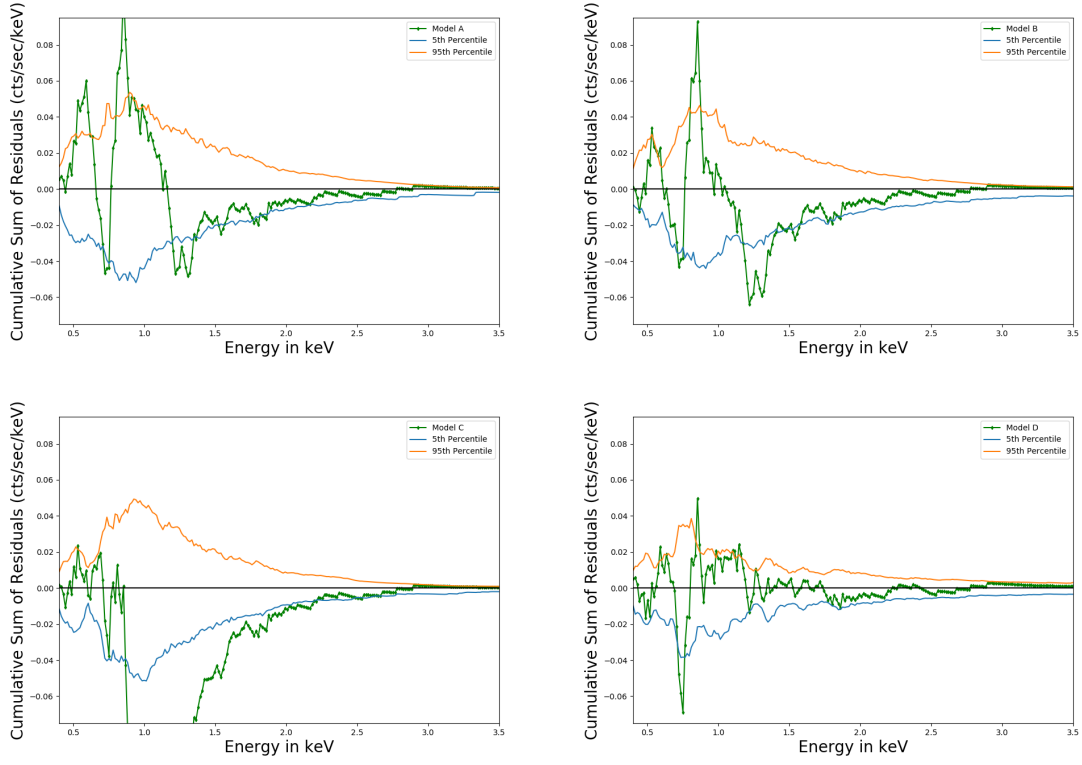


Figure 3.4: Cumulative sum test for the 4 models for observation ID 6120.

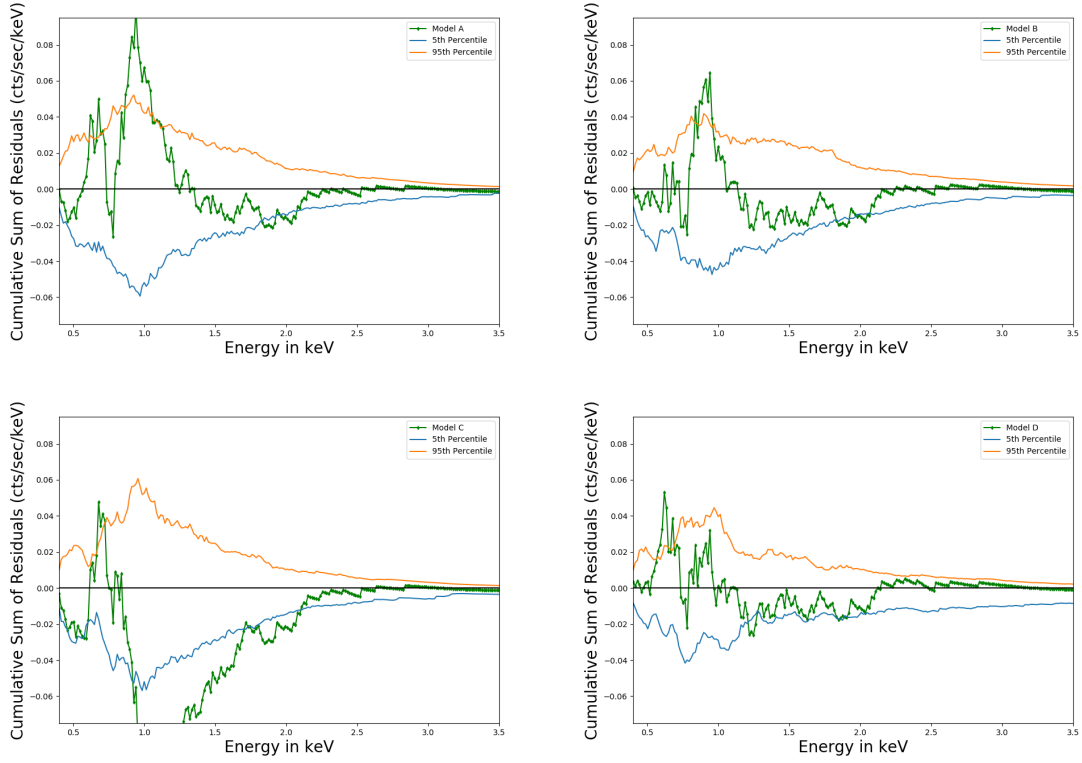


Figure 3.5: Cumulative sum test for the 4 models for observation ID 6121.

3.1.1 Spectral Flux

We also compared the fluxes obtained through these Chandra data sets, and compared them with fluxes reported by past observations using the *Swift* ([D’Elia 13]) and XMM-Newton ([Scandariato 13]) satellites. For doing so, we first scaled all fluxes to the 0.15–4.0 keV regime. Further, as the *Swift* data assumed a 1-temperature model, we assume 3 different temperatures (0.2165 keV, 0.4319 keV, 0.8617 keV) for our comparisons. We also calculate a running mean of the flux versus phase, taking $N=4$ to get an idea about the overall variation. It is important to note that there seems to be evidence of clear flaring in the *Swift* data, which we keep in mind before performing further analyses.

Figure 3.6 shows the variation of flux over time, where time is measured in days from a reference point. This gives us an idea about the spread over which the observations in consideration were carried out. Figure 3.7 shows the variation of flux versus phase, where phase = 0 is the time when the planet is directly between the observer and the star, i.e., along the line of sight. The running mean using the 3 different temperatures for the *Swift* observations is shown as well.

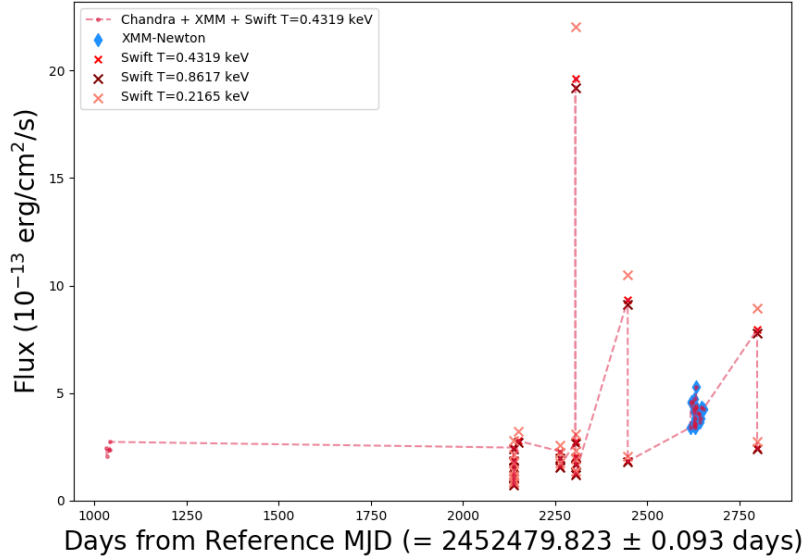


Figure 3.6: Flux versus Time for the Chandra, XMM-Newton and *Swift* observations.

3.1.2 Lomb-Scargle Periodogram

The variation of flux can serve as an important tool to explore the possibility of Star-Planet Interactions. However, even on using data from all 3 satellites, we do not have enough information to establish a clear periodicity. Mainly, the data is not evenly spaced across time,

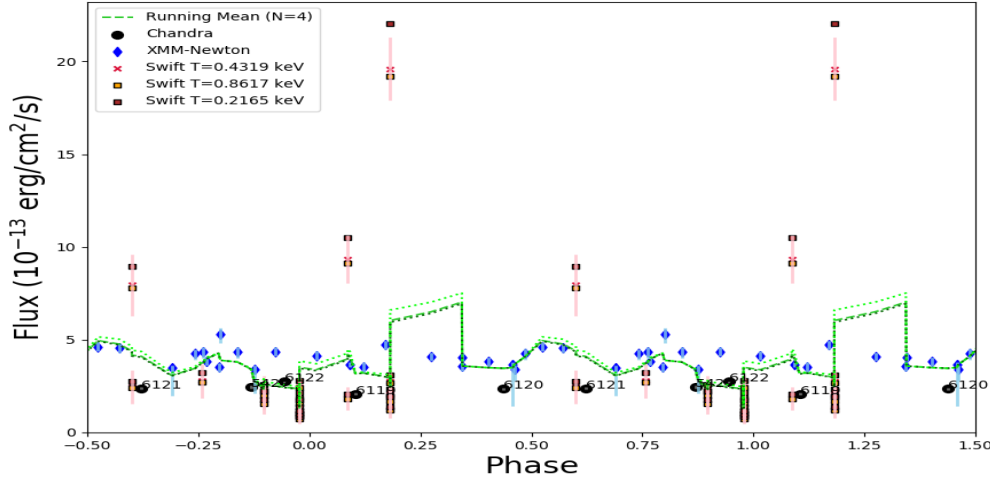


Figure 3.7: Flux versus Phase for the Chandra, XMM-Newton and *Swift* observations, with running mean for $N=4$ shown.

and thus it is difficult to search for periodicity.

Nevertheless, there are methods using which this problem can be sorted. Namely, the Lomb-Scargle ([Scargle 13], [VanderPlas 18]) periodogram is a commonly used statistical tool designed to detect periodic signals in unevenly spaced observations. Before using this technique, we remove the clear flare detected by *Swift* at $\sim 2 \times 10^{-12} \text{ erg s}^{-1} \text{ cm}^{-2}$, as it is a non-periodic event that may cause issues in finding the periodicity. Next, we create a “window function”, which is created assuming a flux of $(1 \pm \tau) \times 10^{-13} + \sigma \text{ erg s}^{-1} \text{ cm}^{-2}$ with τ and σ as randomised errors of the order 0.01 %.

In the Lomb-Scargle periodogram to decide whether a signal contains a periodic component, an important consideration is the *significance* of the periodogram peak. This significance is usually expressed in terms of a false alarm probability (FAP), which encodes the probability of measuring a peak of a given height (or higher) conditioned on the assumption that the data consists of Gaussian noise with no periodic component. We use the method outlined in [Baluev 08] to approximate the 5%, 50% and 95% false alarm probability levels which is showcased in Figure 3.8, along with the Lomb-Scargle periodogram, the window function, and the subtracted periodogram for a Nyquist factor of 50. From the Lomb-Scargle periodogram, it is found that there are possible periodicities of time period 7.94, 7.02, and 3.96 days. There are possible larger time periods as well of the order of ~ 50 days.

From these results, it is indicative that like the chromospheric variation observed in [Scandariato 13], the X-ray output of the stellar corona is more strongly varying with the equatorial stellar

rotational period (which is 7.62 ± 0.05 days), with the 3.96 day periodicity being a possible 2^{nd} harmonic to the periodicity of 7.94 days. However, it cannot be ruled out that the 3.96 day periodicity is a possible periodicity in itself. If that were the case, it highlights the possibility of the X-ray variability being tied to the planet's orbital period, which is 3.09285 ± 0.00056 days. Thus, the Lomb-Scargle periodogram indicates a strong possibility of variation in X-ray output with the stellar rotation period, but does **not** rule out the possibility of star-planet interactions.

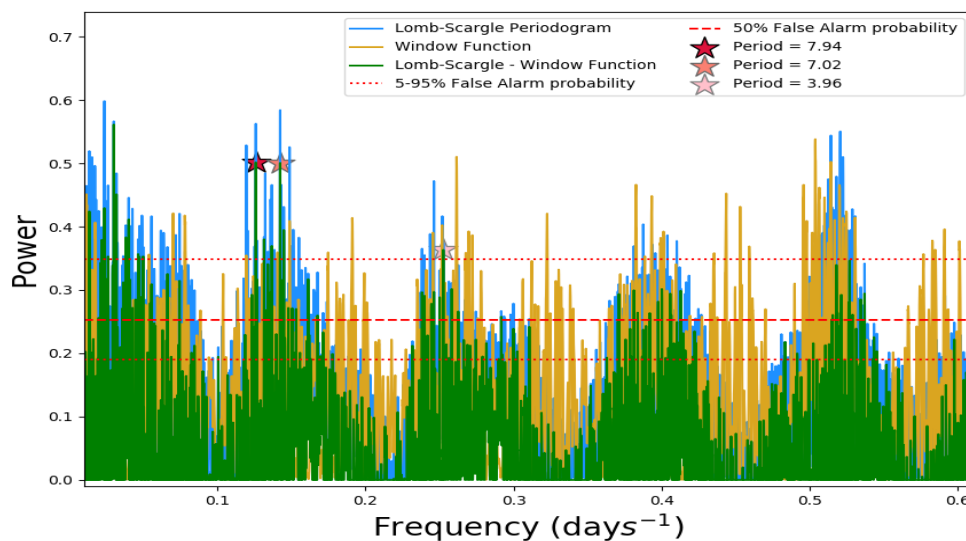


Figure 3.8: Lomb-Scargle periodogram, window function, and the subtracted periodogram for the observed spectral fluxes versus time.

Table 3.6. Passbands:

Energy Range [keV]	Band
0.5 - 0.7	Oxygen band (bandO)
0.7 - 0.9	Fe XVII-XVIII 6 MK band (Fe1718)
0.9 - 1.2	Neon band (bandNe)
1.2 - 3.0	Magnesium band (bandMg)
0.2 - 0.5	Ultrasoft (u)
0.5 - 1.2	Soft (s)
1.2 - 8.0	Medium + Hard (h2)

3.2 Count Rates

The default energy pass bands (ultrasoft, soft, medium and hard) used for Chandra observations is given in Table 3.6. Note that due to low number of counts in the hard passband, it is combined with the medium passband. We also define physically motivated passbands based on the dominant excitation, which is given in Table 3.6 as well.

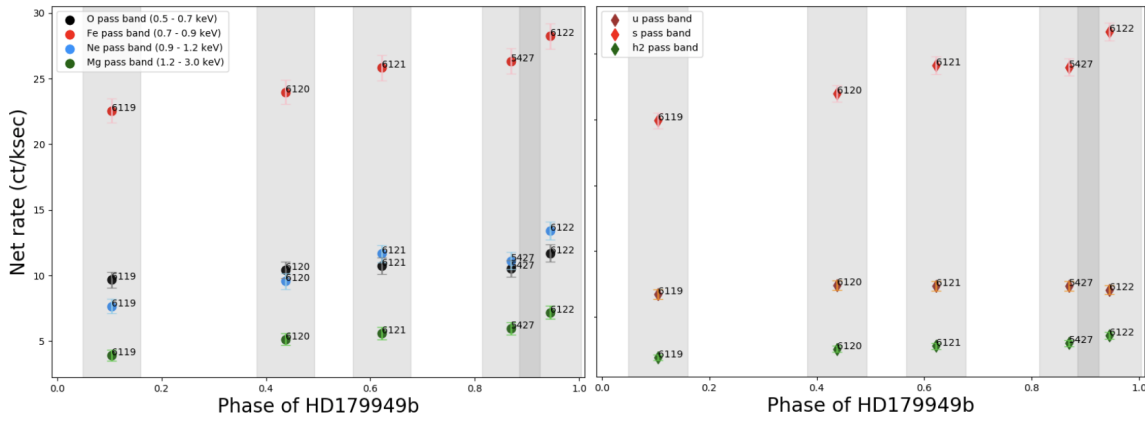


Figure 3.9: Count rates in each passband across all Chandra observation IDs. The grey bars show the exposure duration of each observation.

The physically motivated passbands are named based on the most prominent transitions in the energy range, using the data from [Thompson 09]. Naturally, for this, we focus on the K- α lines, as they are the strongest X-ray spectral line for an element. The K- α lines are the result of electron transitions to the innermost “K” shell (principal quantum number 1) from a 2p orbital of the second or “L” shell (with principal quantum number 2). They are actually doublets (K- α_1 and K- α_2) based on spin-orbit interaction energy differences. The difference arises based on whether the transition is from L₃ (2p_{3/2}) which corresponds to K- α_1 , and L₂ (2p_{1/2}) which corresponds to K- α_2 .

Now, the K- α_1 line for Oxygen corresponds to an energy of 0.525 keV, and thus the 0.5-0.7 keV passband is referred to as the Oxygen band with the shorthand notation of bandO. Similarly, for Neon and Magnesium, the K- α_1 lines are noted based on which the passband names for 0.9 - 1.2 keV and 1.2 - 3.0 keV are assigned. The 0.7 - 0.9 keV passband is named as Fe XVII-XVIII 6 MK band (or Fe1718 in short) because it refers to the pass band that encompasses the transition energies from Fe XVIII (Fe^{17+}) and Fe XVII (Fe^{16+}) to the ground state.

3.3 Light Curves

Another important aspect that we studied were the light curves in various passbands. These show the net count rates across the total time of observation, thus being a good tool to analyse any variability across time. By calculating the phase of the planet during this duration, one can also look for any changes in the net count rates as the phase progresses.

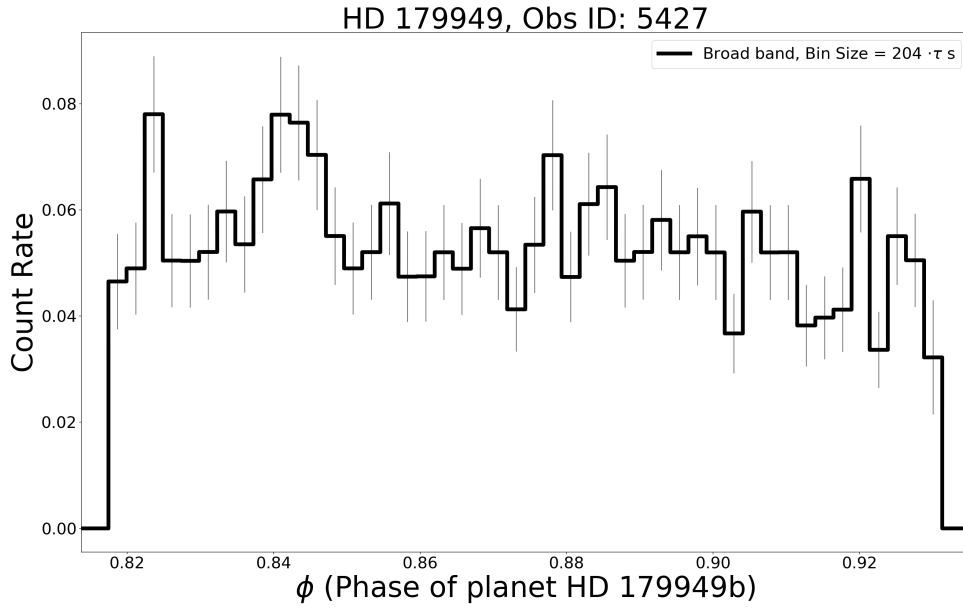


Figure 3.10: Overall light curve in the broad pass band 0.5-7.0 keV with respect to the orbital phase of the planet HD 179949b for observation ID 5427.

However, it is important to ensure proper binning with respect to time, as too narrow bins would start reflecting statistical variations, while too broad bins would miss actual variability. The first thing we noted before binning is the value of TIMEDEL (τ), which is the sum of the static exposure time for a frame (3.2 s) plus the time required to transfer charge from the image region to the frame store region (0.04104 s). For these observations, it is found to

Table 3.7. Optimal bin size for each band, for each ObsID:

ObsID	5427	6119	6120	6121	6122
Passband					
bandO	$340 \cdot \tau$	$460 \cdot \tau$	$272 \cdot \tau$	$420 \cdot \tau$	$284 \cdot \tau$
Fe1718	$328 \cdot \tau$	$270 \cdot \tau$	$264 \cdot \tau$	$356 \cdot \tau$	$284 \cdot \tau$
bandNe	$480 \cdot \tau$	$108 \cdot \tau$	$514 \cdot \tau$	$544 \cdot \tau$	$330 \cdot \tau$
bandMg	$350 \cdot \tau$	$320 \cdot \tau$	$370 \cdot \tau$	$660 \cdot \tau$	$330 \cdot \tau$
u	$384 \cdot \tau$	$440 \cdot \tau$	$402 \cdot \tau$	$544 \cdot \tau$	$354 \cdot \tau$
s	$350 \cdot \tau$	$384 \cdot \tau$	$318 \cdot \tau$	$440 \cdot \tau$	$354 \cdot \tau$
h2	$350 \cdot \tau$	$324 \cdot \tau$	$462 \cdot \tau$	$578 \cdot \tau$	$354 \cdot \tau$

be 3.24104 s. Any binning size shall have to be an integral multiple of this to avoid Moiré patterns.

Next, we proceeded to find the binning size that shall be most appropriate for not losing out on actual variability, while also being able to avoid false interpretations due to statistical error. This optimum binning size was found by calculating the ratio of the expected statistical error and the actual scatter of the number of counts, and note the binning size where it started to drop steadily. This was first used to calculate the optimum binning for the overall energy passband of 0.5-3.0 keV, as shown in Figure 3.10 followed by 4 finer passbands: 0.5-0.7 keV, 0.7-0.9 keV, 0.9-1.2 keV and 1.2-3.0 keV. The optimal binning sizes for all passbands for the 5 observation IDs is given in Table 3.7. Using the optimal binning, we obtain the following light curves shown in Figures 3.11 and 3.12, where we have shown the results for 2 observation IDs 5427 and 6119. The light curves show the variation of count rate with phase of the planet during the observations.

It must be noted that using the light curves to look for variability in X-ray activity as a function of the orbital period may require longer observational periods, or a combination of multiple observations to be comparable with the orbital period. The observation IDs used for the light curves in Figs. 3.11 and 3.12 is only for ~ 0.70 days, which is approximately a fifth of the orbital period.

3.4 Hardness Ratios

The visual evaluation of light curves showcases some variability, however, it is difficult to quantify the variability as actual physical variation, especially when we focus on just one pass band at a time. Further, with different optimal binning for different pass bands, and for different data sets as well, the analysis cannot be done definitively.

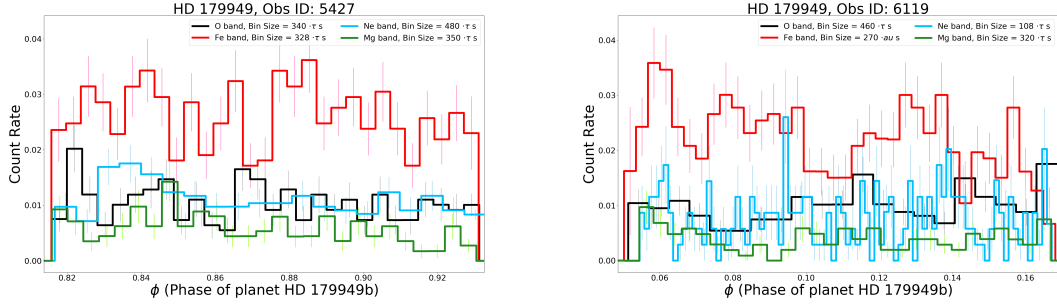


Figure 3.11: Light curve with optimal binning versus phase for the physically motivated passbands.

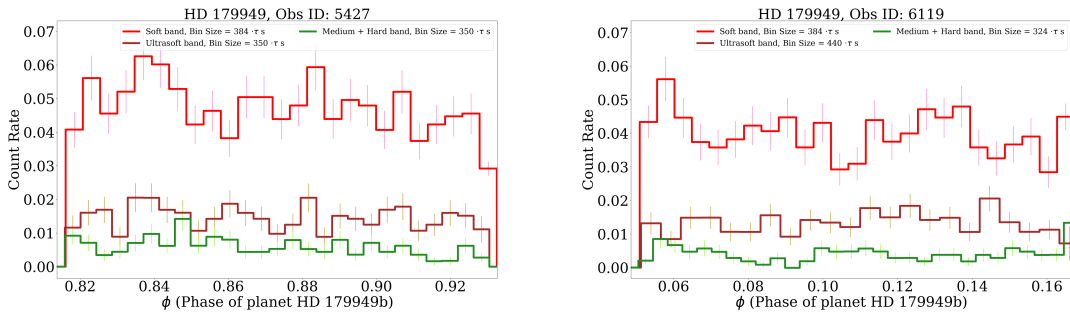


Figure 3.12: Light curve with optimal binning versus phase for the Chandra passbands.

To quantify the variation, we next analysed the results from the light curves to specifically look for variation over time by looking into Hardness Ratios. Hardness Ratio is the equivalent of a photometric color index, and is calculated as a normalized difference of the exposure corrected counts in two energy bands A (high energy), B (low energy). A typical definition is: $HR = \frac{A-B}{A+B}$, but other schemes are also used ([Fruscione 06]).

We used a broader definition, by ignoring the restriction of the A energy band having to be at a higher energy than B. After analysing all possible combinations, we focussed on Hardness Ratios where Fe1718 pass band is taken as the B band, i.e., the *soft* band, with bandO, bandNe and bandMg are taken as the A band, i.e., the *hard* band to calculate hardness ratios. However, for each data set, the pass bands have different optimum time bins. To accommodate this, we used the optimum binning of the A band for binning the B band and vice-versa. To have an understanding of the behaviour when using optimum time bins for both pass bands, we duplicated counts of the narrower bins of one pass band to match broader bins of the other pass band, and then calculated the Hardness Ratios from there. To calculate the Hardness Ratios we use the BEHR (Bayesian Estimation of Hardness Ratios) code, given by [Park 06]. BEHR is a standalone command-line program which is a com-

combination of Fortran and C-based programs. It is designed to quickly estimate the hardness ratios and their uncertainties for astrophysical sources. It is especially useful in the Poisson regime of low counts, and computes the proper uncertainty regardless of whether the source is detected in both passbands or not. This is useful for us, as observations in the X-ray regime tend to follow Poissonian distributions due to low number of photon detections.

On calculating the Hardness Ratios using BEHR, it is observed that the overall variation of hardness ratios with phase is similar in all 3 cases, thus allowing us to use the same binning for both pass bands to analyse the hardness ratios. The Hardness Ratio graphs thus obtained are shown in Figs. 3.13 to 3.21.

To statistically analyse the variation in hardness ratios, we perform the χ^2 test, using the NumPy ([Harris 20]) and SciPy ([Virtanen 20]) packages. From SciPy.stats, we import the *chisquare* function for the same. The results of the χ^2 test are tabulated in Table 3.8. Note that after calculating the χ^2 value, we calculate the number of degrees of freedom, which is equal to the number of points minus the number of variable (here, there is just 1 variable, that is, the hardness ratio). It is to be noted that the first and/or last Hardness Ratio in all cases is -1.0 or $+1.0$ as the beginning of the exposure time does not align exactly with the beginning of observations of the first photons in each passband. Thus, these points are ignored while calculating the degree of freedom.

The expected χ^2 value is then given by $\sqrt{2 \times dof}$, where *dof* is the number of degrees of freedom. A ratio of > 2.0 of the actual χ^2 value and the expected χ^2 value can be taken as an indicator of true X-ray variability. The results thus obtained are tabulated in Table 3.8.

It is interesting to note that all the Hardness Ratios considered in Figs. 3.13 to 3.21 show clear indication of variability. Thus, while it does not immediately clarify the *cause* of the variation, the study of Hardness Ratios confirms that measurable levels of X-ray variability **is occurring** in the stellar corona of HD179949. This provides stronger support to the results obtained from the Lomb-Scargle periodograms, although it does not confirm or deny the existence of star-planet interactions.

Table 3.8. χ^2 Test for the calculated Hardness Ratios, for each ObsID:

Passbands Used \ ObsID	Binning Used	Parameter	5427	6119	6120	6121	6122
Fe1718 vs bandMg	bandMg (“Hard”)	χ^2	27.30	26.72	25.20	13.56	31.00
		dof	27	29	24	13	29
		$\chi^2/\sqrt{2 \times dof}$	3.72	3.51	3.64	2.66	4.07
	Fe1718 (“Soft”)	χ^2	26.88	34.44	39.25	29.18	28.28
		dof	27	35	34	24	34
		$\chi^2/\sqrt{2 \times dof}$	3.66	4.12	4.76	4.21	3.71
Fe1718 vs bandNe	bandNe (“Hard”)	χ^2	14.66	68.58	39.53	14.24	32.05
		dof	18	90	17	16	29
		$\chi^2/\sqrt{2 \times dof}$	2.44	5.11	6.78	2.52	4.21
	Fe1718 (“Soft”)	χ^2	21.72	30.50	46.69	21.85	23.22
		dof	27	35	34	24	34
		$\chi^2/\sqrt{2 \times dof}$	2.96	3.65	5.66	3.15	2.82
Fe1718 vs bandO	bandO (“Hard”)	χ^2	28.12	38.33	17.04	17.04	35.64
		dof	27	19	33	21	34
		$\chi^2/\sqrt{2 \times dof}$	3.83	5.76	4.72	2.63	4.32
	Fe1718 (“Soft”)	χ^2	30.29	49.38	38.95	15.36	...
		dof	27	34	34	25	...
		$\chi^2/\sqrt{2 \times dof}$	4.12	5.99	4.72	2.17	...

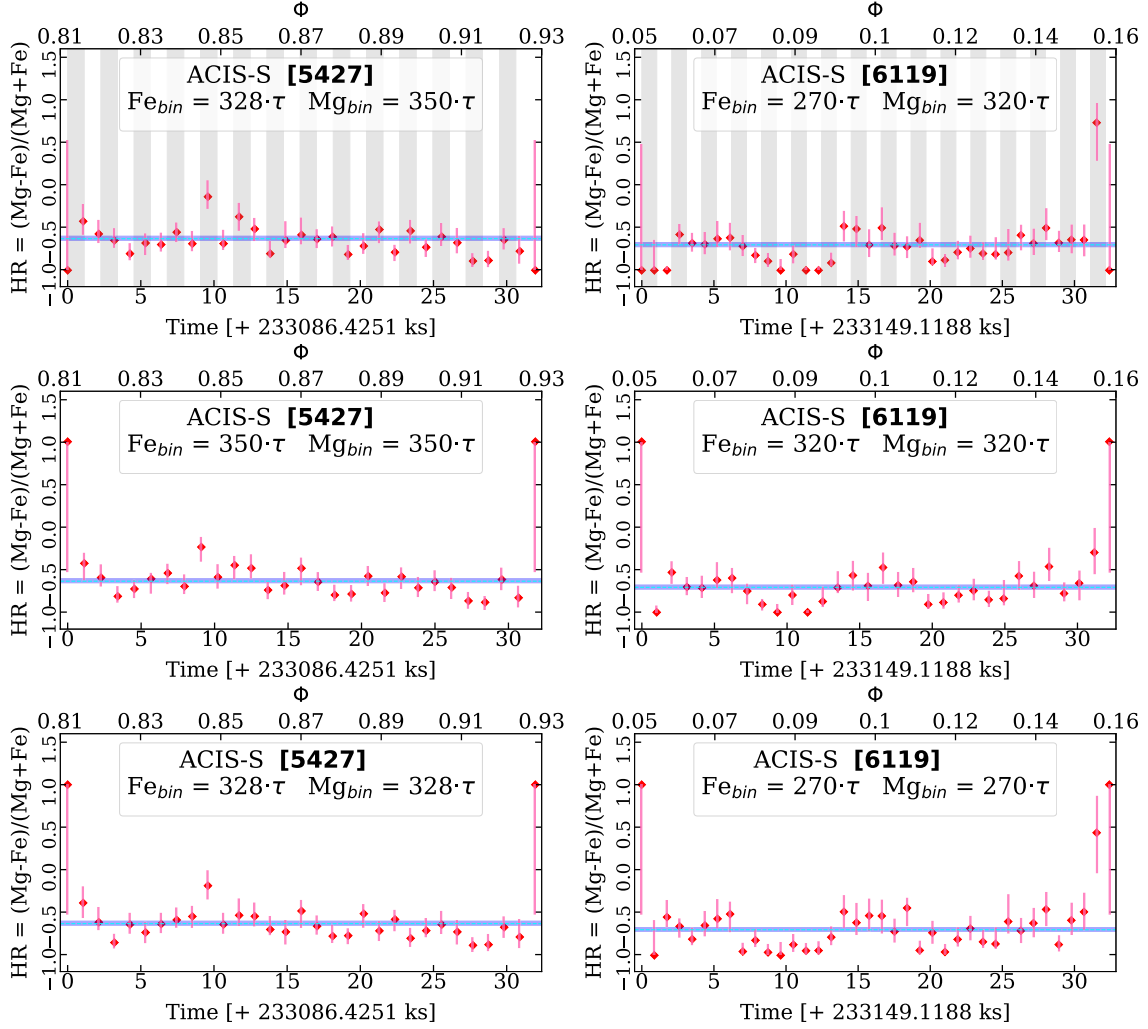


Figure 3.13: Hardness Ratio (HR) graphs for the Fe1718 and bandMg (including Silicon, Aluminium and Sulphur) pass bands for the observation IDs 5427 and 6119.

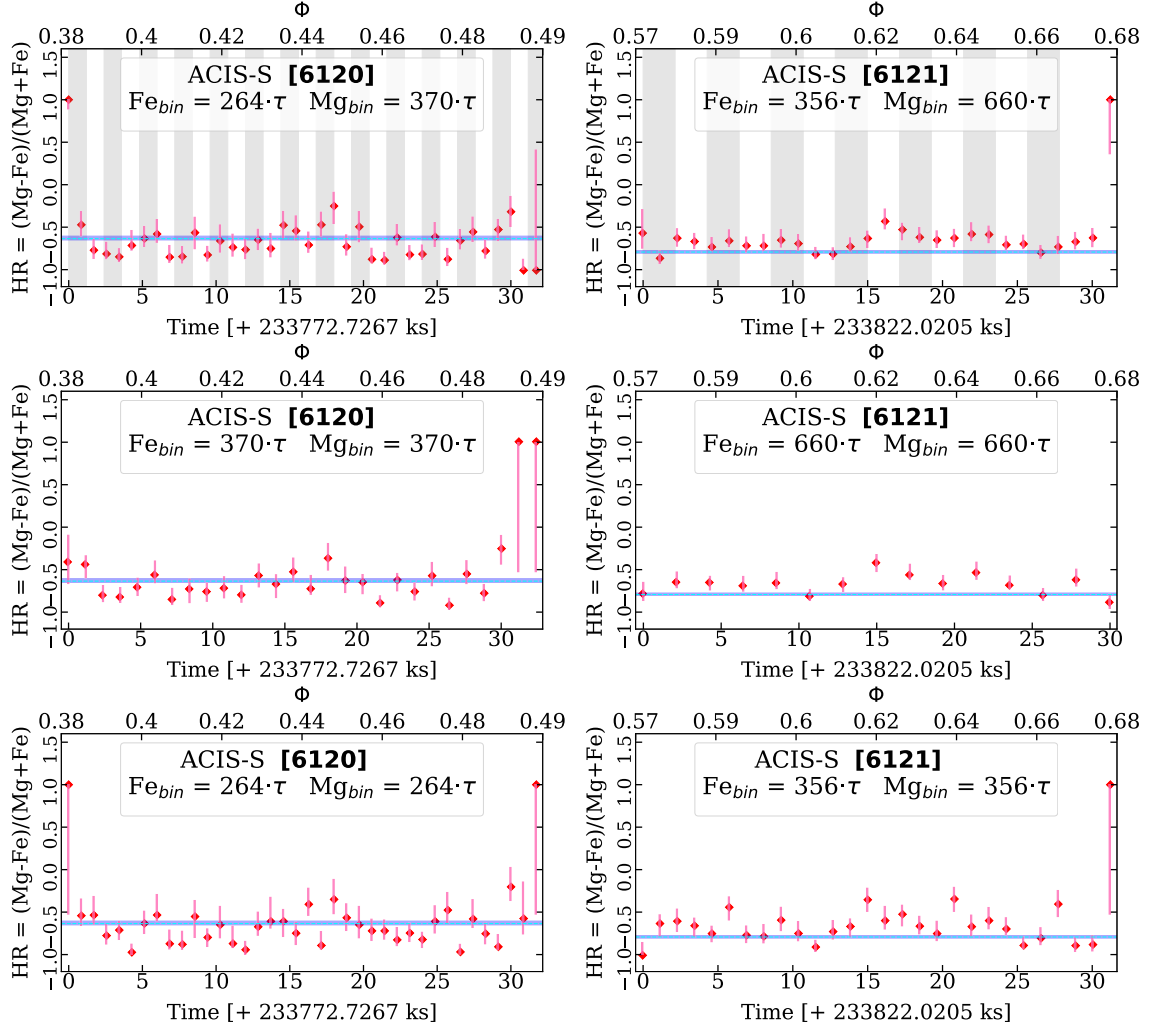


Figure 3.14: Hardness Ratio (HR) graphs for the Fe1718 and bandMg (including Silicon, Aluminium and Sulphur) pass bands for the observation IDs 6120 and 6121.

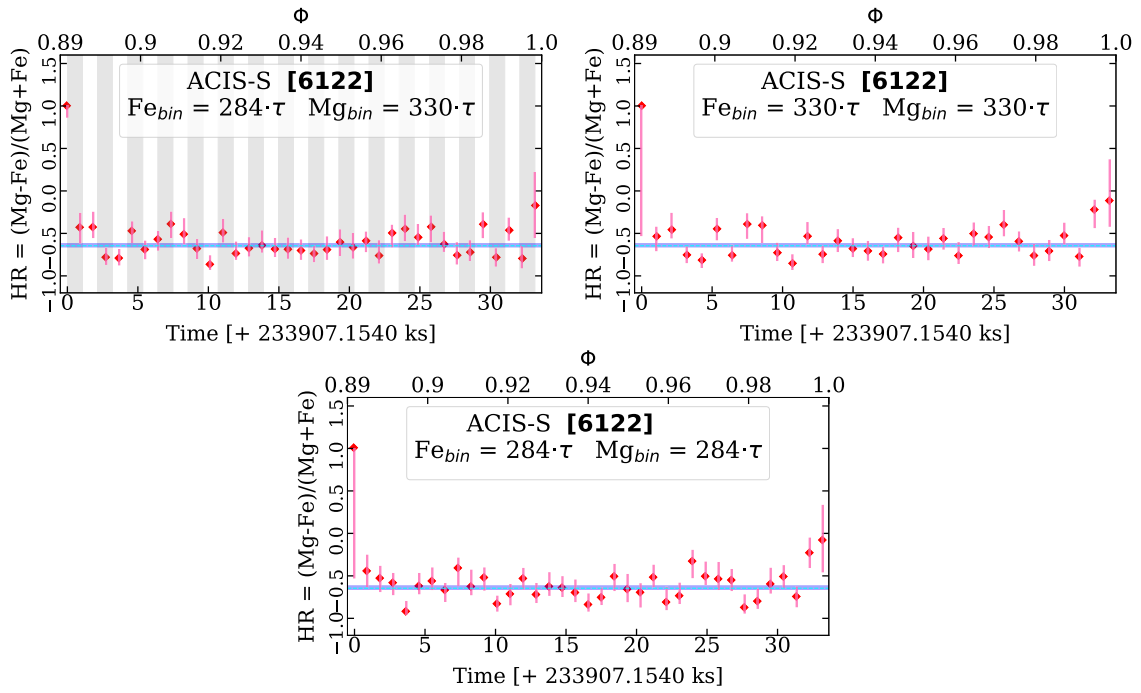


Figure 3.15: Hardness Ratio (HR) graphs for the Fe1718 and bandMg (including Silicon, Aluminium and Sulphur) pass bands for the observation IDs 6122.

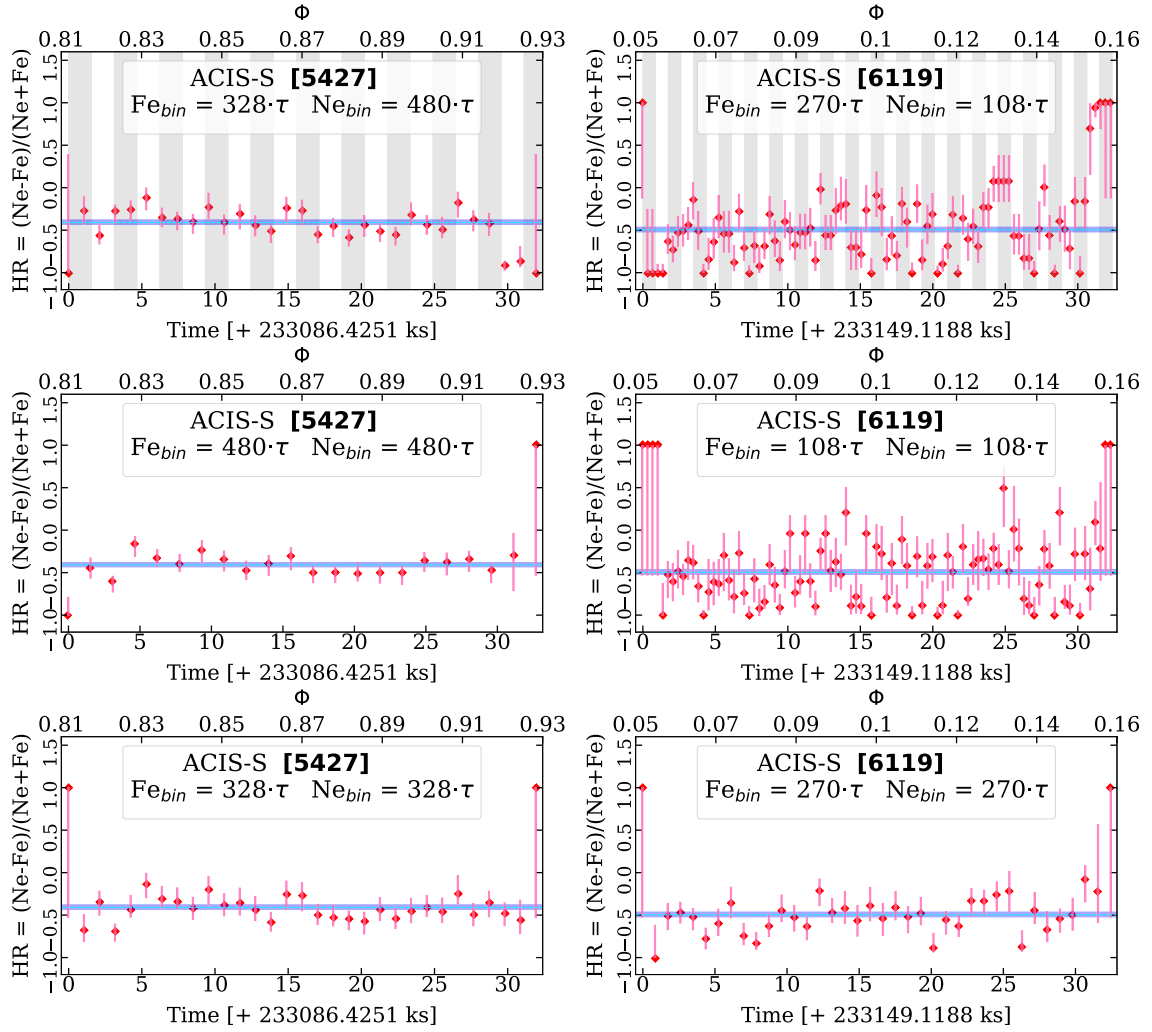


Figure 3.16: Hardness Ratio (HR) graphs for the Fe1718 and bandNe pass bands for the observation IDs 5427 and 6119.

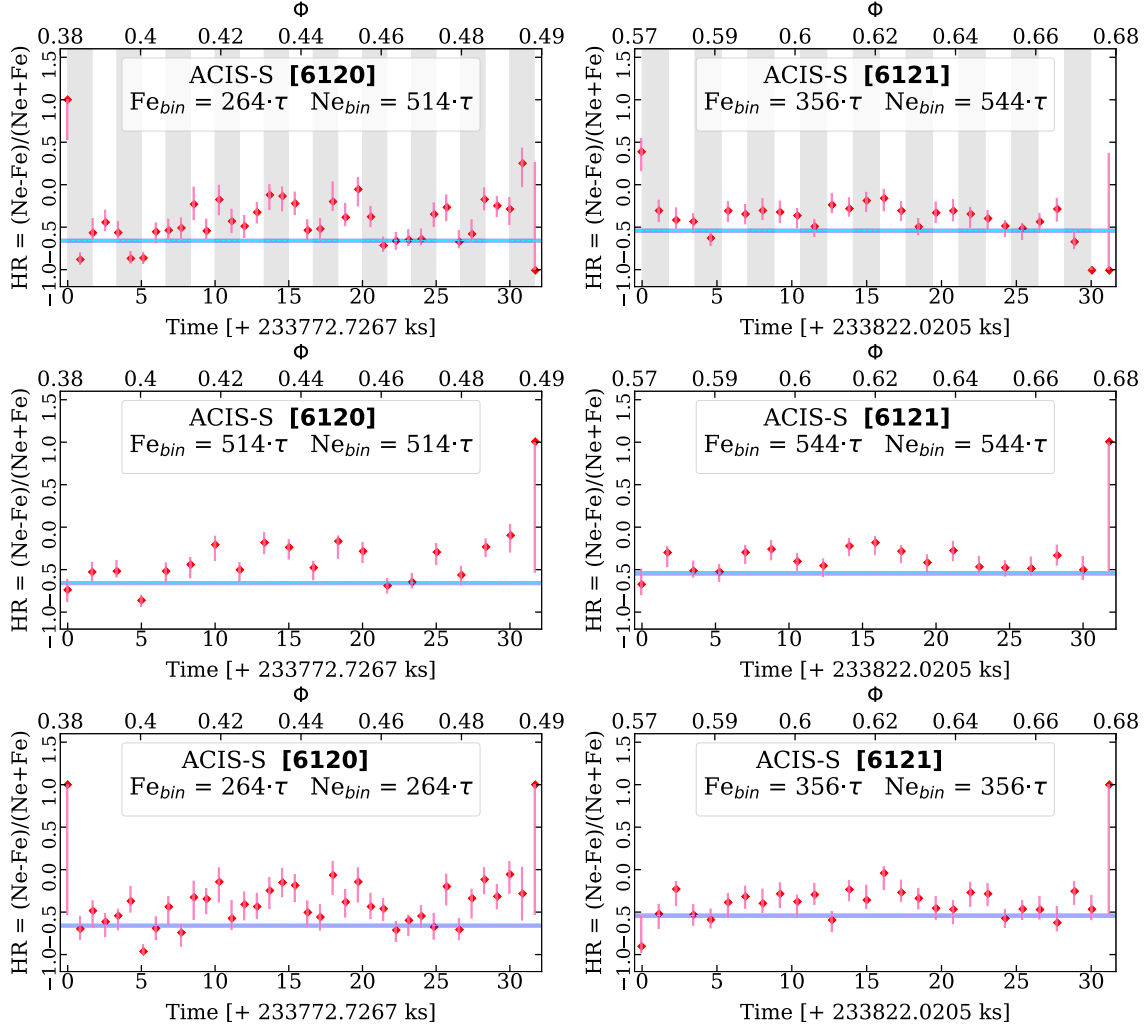


Figure 3.17: Hardness Ratio (HR) graphs for the Fe1718 and bandNe pass bands for the observation IDs 6120 and 6121.

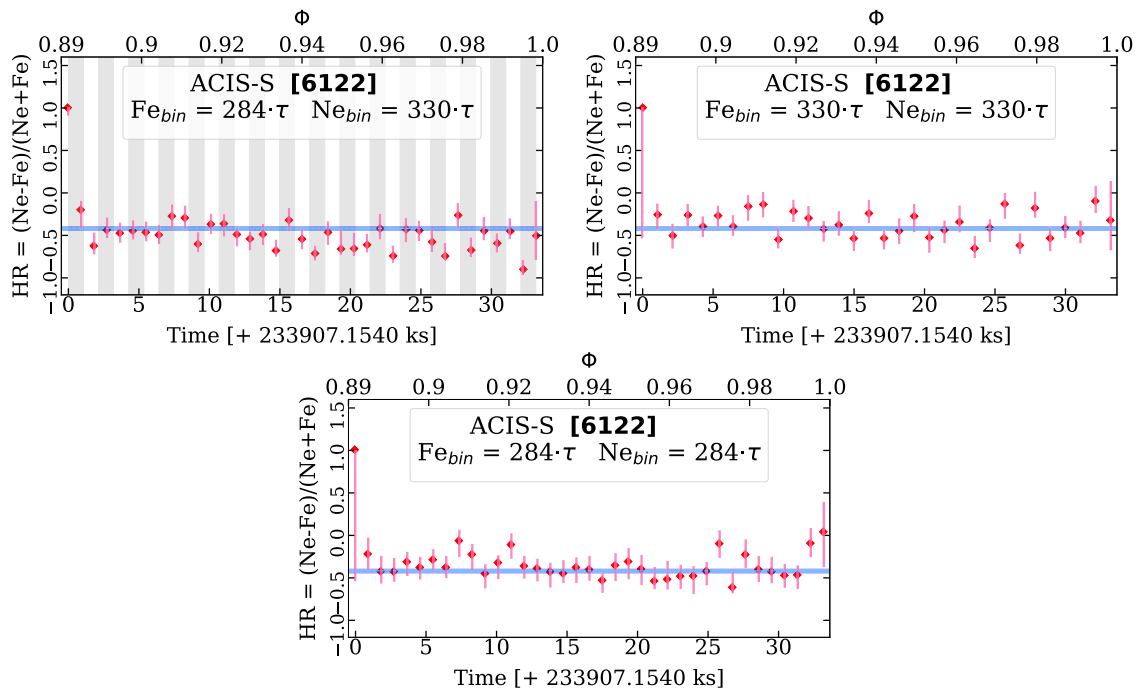


Figure 3.18: Hardness Ratio (HR) graphs for the Fe1718 and bandNe pass bands for the observation IDs 6122.

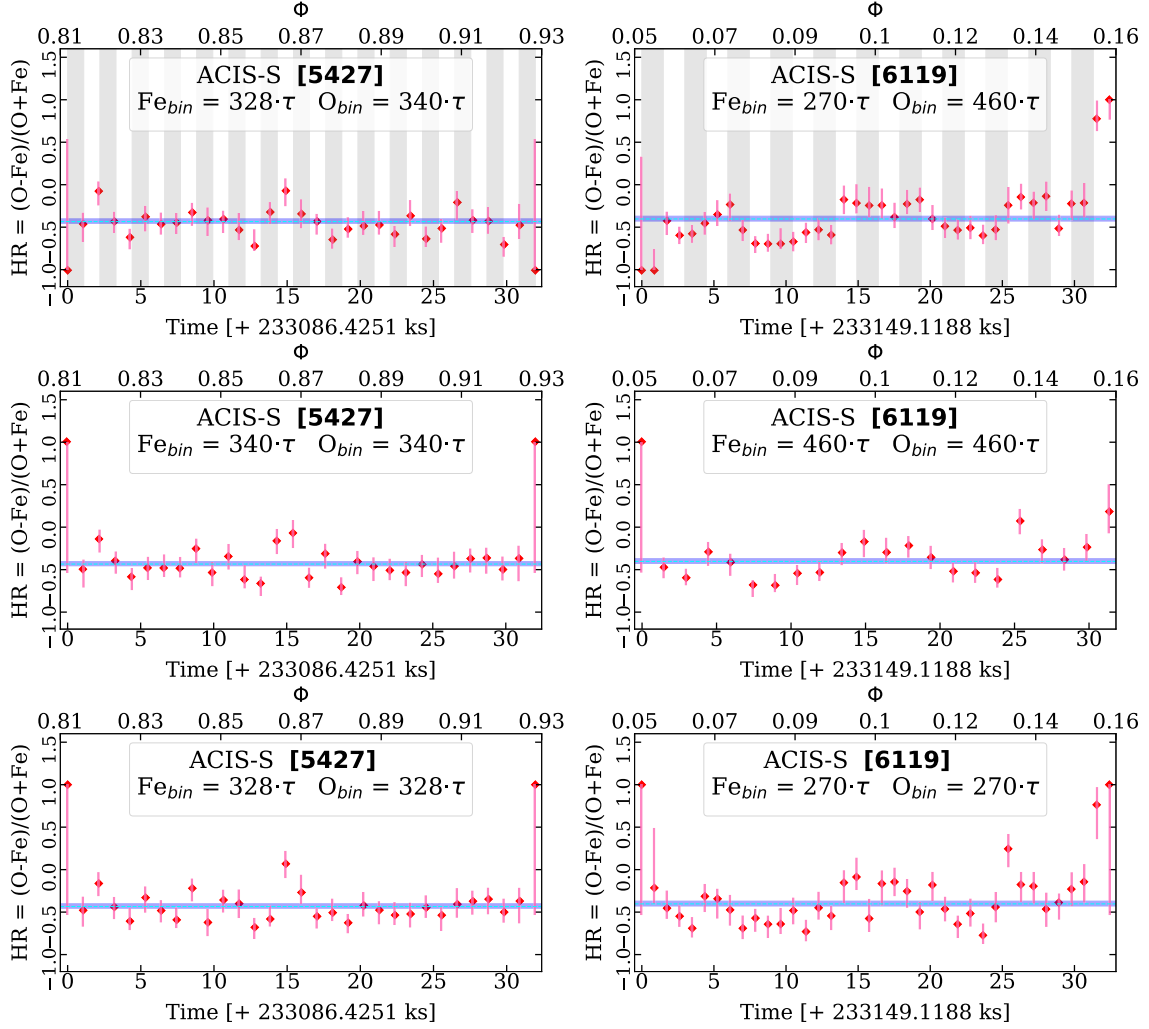


Figure 3.19: Hardness Ratio (HR) graphs for the Fe1718 and bandO pass bands for the observation IDs 5427 and 6119.

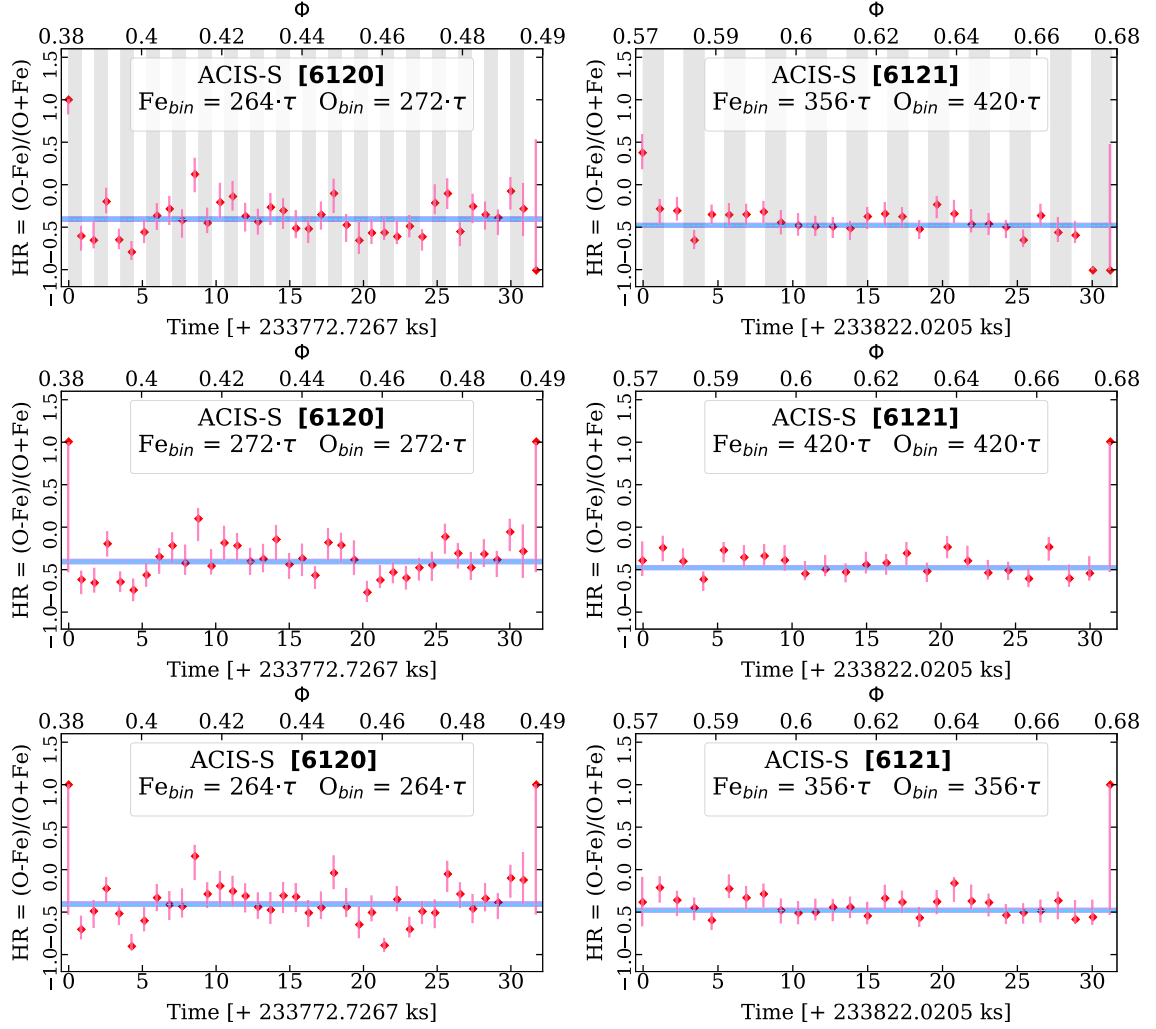


Figure 3.20: Hardness Ratio (HR) graphs for the Fe1718 and bandO pass bands for the observation IDs 6120 and 6121.

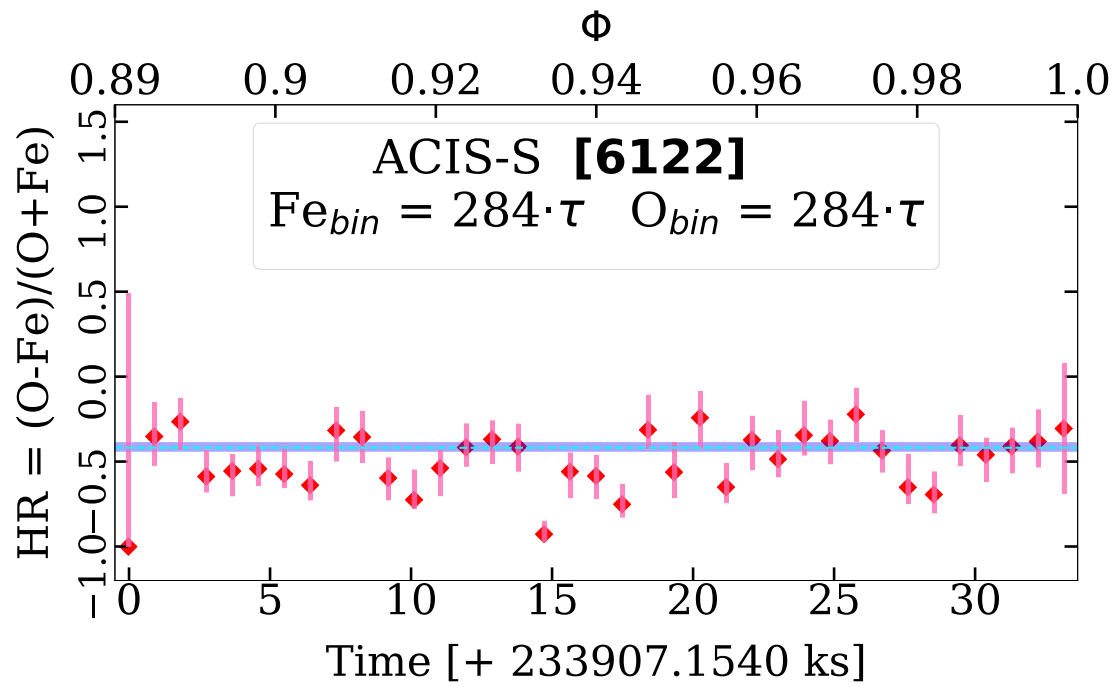


Figure 3.21: Hardness Ratio (HR) graphs for the Fe1718 and bandO pass bands for the observation IDs 6122. Note that as pass bands Fe1718 and bandO have the same optimal binning of 284τ , there are no graphs for translating the hard band's binning to the soft band's binning and vice-versa.

Chapter 4

Results and Discussion

The work done in this project allows us to conclude the following:

- The 2-component nudged abundance model (Model D) is a reasonable approximation of the spectra observed.
- From Model D, there is evidence that the abundance of Aluminium and Nitrogen is higher than the solar photospheric abundance.
- At the same time, low abundance of Calcium, and other metals is noted as compared to the chromospheric abundance estimates in [Scandariato 13].
- Iron abundance is slightly lower ($\sim 0.4 \text{ Fe}_{\odot}$) than the measured photospheric values by [Scandariato 13].
- Oxygen abundance is slightly higher ($\text{O/Fe} \sim 0.6$), than the measured chromospheric values by [Scandariato 13].
- Neon abundance is low but with large error bars ($\text{Ne/Fe} = 0.05 - 1.0$).
- Median Silicon abundance is similar to [Scandariato 13] but with large variation.
- Evaluation of Hardness Ratios with the Fe1718 passband as the “softer” band and the other physically motivated passbands as the “harder” bands showcases clear variability of the X-ray emission from the stellar corona.
- The Lomb-Scargle periodogram suggests the periodicity of flux variation to be tied to the stellar rotation (agreeing with the result of $P_{rot} = 7$ days for two of the 6 observation epochs of [Shkolnik 07]), however, there is also evidence suggesting the possibility of dependence on the orbital period of the planet HD179949b.

Chapter 5

Summary

On studying the 5 data sets from the Chandra X-ray Observatory comprising about half the orbit of the planet HD179949b around its parent star HD179949 (~ 1.74 days) allows us to successfully conclude that the stellar corona showcases variability in its X-ray emission. This is an expected result for a Sun-like star, and we are able to get a measure of the extent of the variability by studying the Hardness Ratios. However, on analysing the Lomb-Scargle periodograms, it is **not** possible for us to conclude that the variability is due to Star-Planet Interactions. In fact, we are able to see stronger proof for the periodicity of variation being tied to the equatorial rotational period of the star, as had been concluded by chromospheric emission studies, on combining our results with those from XMM-Newton and Swift.

The 2-component model with nudged abundances is a reasonable approximation of the spectra of the stellar corona observed. It definitely still has scope for improvement, specifically in the low energy region of 0.4 - 0.7 keV. Nevertheless the properties it reflects are a good starting point to understand the nature of the coronal X-ray activity.

However, the differences between the coronal and chromospheric abundances suggest that the FIP and reverse FIP effects are at play for this star as well. However, the behaviour is not exactly the same as observed for the Solar FIP effect, as while the abundance of Aluminium and other similar metals is higher in the coronal region, Nitrogen is also shown to have higher abundance. Further, it is noted that the fraction of the surface area of the star covered by the hotter component is $\sim 5\%$, while the cooler component covers $\sim 8.5\%$. Variations in the temperatures of the 2 components across the data sets is also observed, which is explained by the observed X-ray variability.

However, no definitive existence of Star-Planet Interactions is observed. We can also not

rule it out completely based on the data we have at hand. It must be noted that we have disjointed observations just covering half the orbit of the planet. Thus, it would be helpful to gather more observations using Chandra and AstroSat and comparing the data with the results we have obtained so far. Stitching all the datasets together and analysing the overall spectra after subtracting flares can be an interesting approach as well once we have more observations. With the current data, we have an idea about the lower limit of exposure time that we need. This work also provides a basis for applying for future proposals to Chandra, XMM-Newton and AstroSat.

Bibliography

- [Anders 89] Edward Anders & Nicolas Grevesse. *Abundances of the elements: Meteoritic and solar*. *Geochimica et Cosmochimica Acta*, vol. 53, no. 1, pages 197–214, 1989.
- [Anderson 12] E. Anderson & Ch. Francis. *XHIP: An extended hipparcos compilation*. *Astronomy Letters*, vol. 38, no. 5, page 331–346, May 2012.
- [Arnaud 96] K. A. Arnaud. *XSPEC: The First Ten Years*. *Astronomical Society of the Pacific Conference Series*, vol. 101, page 17, Dec 1996.
- [Ballesteros 19] F.J. Ballesteros, A. Fernandez-Soto & V.J. Martínez. *Diving into Exoplanets: Are Water Seas the Most Common?* *Astrobiology*, vol. 19, no. 5, pages 642–654, 2019. PMID: 30789285.
- [Baluev 08] R. V. Baluev. *Assessing the statistical significance of periodogram peaks*. *Monthly Notices of the Royal Astronomical Society*, vol. 385, no. 3, page 1279–1285, Apr 2008.
- [Bonfanti 15] A. Bonfanti, S. Ortolani & V. Nascimbeni. *Age consistency between exoplanet hosts and field stars*. *Astronomy & Astrophysics*, vol. 585, page A5, Dec 2015.
- [Brickhouse 00] N. Brickhouse, Randall Smith, J. Raymond & D. Liedahl. *The Astrophysical Plasma Emission Code*. 01 2000.
- [Butler 06] R. P. Butler, J. T. Wright, G. W. Marcy, D. A. Fischer, S. S. Vogt, C. G. Tinney, H. R. A. Jones, B. D. Carter, J. A. Johnson, C. McCarthy & et al. *Catalog of Nearby Exoplanets*. *The Astrophysical Journal*, vol. 646, no. 1, page 505–522, Jul 2006.
- [Cauley 19] P. Wilson Cauley, Evgenya L. Shkolnik, Joe Llama & Antonino F. Lanza. *Magnetic field strengths of hot Jupiters from signals of*

star–planet interactions. Nature Astronomy, vol. 3, no. 12, page 1128–1134, Jul 2019.

- [D’Elia 13] V. D’Elia, M. Perri, S. Puccetti, M. Capalbi, P. Giommi, D. N. Burrows, S. Campana, G. Tagliaferri, G. Cusumano, P. Evans & et al. *The seven year Swift-XRT point source catalog (1SWXRT)*. Astronomy Astrophysics, vol. 551, page A142, Mar 2013.
- [Exoplanet.eu 21] Exoplanet.eu. *The Extrasolar Planets Encyclopaedia*, 2021.
- [Fares 12] R. Fares, J.-F. Donati, C. Moutou, M. Jardine, A. C. Cameron, A. F. Lanza, D. Bohlender, S. Dieters, A. F. Martínez Fiorenzano, A. Maggio & et al. *Magnetic field, differential rotation and activity of the hot-Jupiter-hosting star HD 179949*. Monthly Notices of the Royal Astronomical Society, vol. 423, no. 2, page 1006–1017, May 2012.
- [Foster 16] Adam Foster, N. S. Smith R. K. and Brickhouse & X. Cui. Atomdb and pyatomdb: Atomic data and modelling tools for high energy and non-maxwellian plasmas. 2016.
- [Fruscione 06] Antonella Fruscione, Jonathan C. McDowell, Glenn E. Allen, Nancy S. Brickhouse, Douglas J. Burke, John E. Davis, Nick Durham, Martin Elvis, Elizabeth C. Galle, Daniel E. Harris, David P. Huenemoerder, John C. Houck, Bish Ishibashi, Margarita Karovska, Fabrizio Nicastro, Michael S. Noble, Michael A. Nowak, Frank A. Primini, Aneta Siemiginowska, Randall K. Smith & Michael Wise. *CIAO: Chandra’s data analysis system*. In David R. Silva & Rodger E. Doxsey, editors, Observatory Operations: Strategies, Processes, and Systems, volume 6270, pages 586 – 597. International Society for Optics and Photonics, SPIE, 2006.
- [Gaia Collaboration 18] Gaia Collaboration & Brown, A. G. A., et al. *Gaia Data Release 2 - Summary of the contents and survey properties*. A&A, vol. 616, page A1, 2018.
- [Glesener 17] Lindsay Glesener, Säm Krucker, Iain G. Hannah, Hugh Hudson, Brian W. Grefenstette, Stephen M. White, David M. Smith & Andrew J. Marsh. *NuSTAR Hard X-Ray Observation of a Sub-A Class*

- Solar Flare*. The Astrophysical Journal, vol. 845, no. 2, page 122, aug 2017.
- [Guedel 04] Manuel Guedel. *X-ray astronomy of stellar coronae*. The Astronomy and Astrophysics Review, vol. 12, no. 2-3, Sep 2004.
- [Gurdemir 12] L. Gurdemir, S. Redfield & M. Cuntz. *Planet-Induced Emission Enhancements in HD 179949: Results from McDonald Observations*. Publications of the Astronomical Society of Australia, vol. 29, no. 2, page 141–149, 2012.
- [Harris 20] Charles R. Harris, K. Jarrod Millman, St’efan J. van der Walt, Ralf Gommers, Pauli Virtanen, David Cournapeau, Eric Wieser, Julian Taylor, Sebastian Berg, Nathaniel J. Smith, Robert Kern, Matti Picus, Stephan Hoyer, Marten H. van Kerkwijk, Matthew Brett, Allan Haldane, Jaime Fern’andez del R’io, Mark Wiebe, Pearu Peterson, Pierre G’erard-Marchant, Kevin Sheppard, Tyler Reddy, Warren Weckesser, Hameer Abbasi, Christoph Gohlke & Travis E. Oliphant. *Array programming with NumPy*. Nature, vol. 585, no. 7825, pages 357–362, September 2020.
- [Høg 00] Erik Høg, C. Fabricius, Valeri Makarov, S. Urban, G. Wycoff, U. Bastian, P. Schwekendiek & Andreas Wicenec. *The Tycho-2 Catalogue of the 2.5 million brightest stars*. Astronomy and Astrophysics, vol. 355, pages L27–L30, 02 2000.
- [Kaastra 17] J. S. Kaastra. *On the use of C-stat in testing models for X-ray spectra*. Astronomy & Astrophysics, vol. 605, page A51, Sep 2017.
- [Kashyap 98] Vinay Kashyap & Jeremy J. Drake. *Markov-Chain Monte Carlo Reconstruction of Emission Measure Distributions: Application to Solar Extreme-Ultraviolet Spectra*. The Astrophysical Journal, vol. 503, no. 1, pages 450–466, Aug 1998.
- [Kashyap 08] Vinay L. Kashyap, Jeremy J. Drake & Steven H. Saar. *Extrasolar Giant Planets and X-Ray Activity*. The Astrophysical Journal, vol. 687, no. 2, page 1339–1354, Nov 2008.
- [Laming 15] J. Martin Laming. *The FIP and Inverse FIP Effects in Solar and Stellar Coronae*. Living Reviews in Solar Physics, vol. 12, no. 1, Sep 2015.

- [Lee 11] N. P. Lee. An X-ray Data Primer. 2011.
- [Neal 93] R. M. Neal. Probabilistic Inference Using Markov Chain Monte Carlo Methods. 1993.
- [Park 06] Taeyoung Park, Vinay L. Kashyap, Aneta Siemiginowska, David A. van Dyk, Andreas Zezas, Craig Heinke & Bradford J. Wargelin. *Bayesian Estimation of Hardness Ratios: Modeling and Computations*. The Astrophysical Journal, vol. 652, no. 1, page 610–628, Nov 2006.
- [Saar 07] S. H. Saar, M. Cuntz, V. L. Kashyap & J. C. Hall. *First observation of planet-induced X-ray emission: The system HD 179949*. Proceedings of the International Astronomical Union, vol. 3, no. S249, page 79–81, Oct 2007.
- [Scandariato 13] G. Scandariato, A. Maggio, A. F. Lanza, I. Pagano, R. Fares, E. L. Shkolnik, D. Bohlender, A. C. Cameron, S. Dieters, J.-F. Donati & et al. *A coordinated optical and X-ray spectroscopic campaign on HD 179949: searching for planet-induced chromospheric and coronal activity*. Astronomy & Astrophysics, vol. 552, page A7, Mar 2013.
- [Scargle 13] Jeffrey D. Scargle, Jay P. Norris, Brad Jackson & James Chiang. *STUDIES IN ASTRONOMICAL TIME SERIES ANALYSIS. VI. BAYESIAN BLOCK REPRESENTATIONS*. The Astrophysical Journal, vol. 764, no. 2, page 167, Feb 2013.
- [Shkolnik 04] E. Shkolnik, G. A. H. Walker & D. A. Bohlender. *Erratum: “Evidence for Planet-induced Chromospheric Activity on HD 179949” (ApJ, 597, 1092 [2003])*. The Astrophysical Journal, vol. 609, no. 2, page 1197–1197, Jul 2004.
- [Shkolnik 07] Evgenya Shkolnik, David A. Bohlender, Gordon A. H. Walker & Andrew Collier Cameron. *The On/Off nature of star-planet interactions in the HD 179949 and υ And systems*. Proceedings of the International Astronomical Union, vol. 3, no. S249, page 151–158, 2007.
- [Smith 01] Randall K. Smith, Nancy S. Brickhouse, Duane A. Liedahl & John C. Raymond. *Collisional Plasma Models with APEC/APED*:

Emission-Line Diagnostics of Hydrogen-like and Helium-like Ions. The Astrophysical Journal, vol. 556, no. 2, page L91–L95, Aug 2001.

- [Soubiran, C. 18] Soubiran, C., Jasiewicz, G., Chemin, L., Zurbach, C., Brouillet, N., Panuzzo, P., Sartoretti, P., Katz, D., Le Campion, J.-F., Marchal, O., Hestroffer, D., Thévenin, F., Crifo, F., Udry, S., Cropper, M., Seabroke, G., Viala, Y., Benson, K., Blomme, R., Jean-Antoine, A., Huckle, H., Smith, M., Baker, S. G., Damerджи, Y., Dolding, C., Frémat, Y., Gosset, E., Guerrier, A., Guy, L. P., Haigron, R., Janßen, K., Plum, G., Fabre, C., Lasne, Y., Pailer, F., Panem, C., Riclet, F., Royer, F., Tauran, G., Zwitter, T., Gueguen, A. & Turon, C. *Gaia Data Release 2 - The catalogue of radial velocity standard stars*. A&A, vol. 616, page A7, 2018.
- [Speagle 20] Joshua S. Speagle. *A Conceptual Introduction to Markov Chain Monte Carlo Methods*, 2020.
- [Thompson 09] A. C. Thompson. X-Ray Data Booklet. 2009.
- [van Dyk 01] David A. van Dyk, Alanna Connors, Vinay L. Kashyap & Aneta Siemiginowska. *Analysis of Energy Spectra with Low Photon Counts via Bayesian Posterior Simulation*. The Astrophysical Journal, vol. 548, no. 1, page 224–243, Feb 2001.
- [VanderPlas 18] Jacob T. VanderPlas. *Understanding the Lomb–Scargle Periodogram*. The Astrophysical Journal Supplement Series, vol. 236, no. 1, page 16, May 2018.
- [Virtanen 20] Pauli Virtanen, Ralf Gommers, Travis E. Oliphant, Matt Haberland, Tyler Reddy, David Cournapeau, Evgeni Burovski, Pearu Peterson, Warren Weckesser, Jonathan Bright, Stéfan J. van der Walt, Matthew Brett, Joshua Wilson, K. Jarrod Millman, Nikolay Mayorov, Andrew R. J. Nelson, Eric Jones, Robert Kern, Eric Larson, C J Carey, İlhan Polat, Yu Feng, Eric W. Moore, Jake VanderPlas, Denis Laxalde, Josef Perktold, Robert Cimrman, Ian Henriksen, E. A. Quintero, Charles R. Harris, Anne M. Archibald, Antônio H. Ribeiro, Fabian Pedregosa, Paul van Mulbregt & SciPy 1.0 Contributors. *SciPy 1.0: Fundamental Al-*

gorithms for Scientific Computing in Python. Nature Methods, vol. 17, pages 261–272, 2020.

- [Viswanath 20] Gayathri Viswanath, Mayank Narang, P Manoj, Blesson Mathew & Sreeja S Kartha. *A Statistical Search for Star–Planet Interaction in the Ultraviolet Using GALEX*. The Astronomical Journal, vol. 159, no. 5, page 194, Apr 2020.
- [Wang 11] Ji Wang & Eric B. Ford. *On the eccentricity distribution of short-period single-planet systems*. Monthly Notices of the Royal Astronomical Society, vol. 418, no. 3, page 1822–1833, Sep 2011.
- [Wittenmyer 08] Rob Wittenmyer, Michael Endl & and Cochran. *Long-Period Objects in the Extrasolar Planetary Systems 47 Ursae Majoris and 14 Herculis*. The Astrophysical Journal, vol. 654, page 625, Dec 2008.
- [Wolszczan 92] A. Wolszczan & D. A. Frail. "A planetary system around the millisecond pulsar PSR1257 + 12" (*Nature*, 355, 145–147 [1992]). Nature, vol. 355, no. 2, Jan 1992.

Chapter 6

Appendix

A.1 Color

Instead of studying the evolution of Hardness Ratios over time for the observations, we can also use Color, which is defined as $C = \log_{10}(B/A)$, where B and A are the two pass bands being studied. Color can be an important tool to analyse the behaviour of the light curves, especially when there is high amount of variation, as the log scale aids in making it comparable. However, as that is not the case here, we have used Hardness Ratios for performing the χ^2 test. The evolution of Color with time and phase of orbit for observation IDs 5427 and 6119 is shown in Figs. 6.1, 6.2 and 6.3.

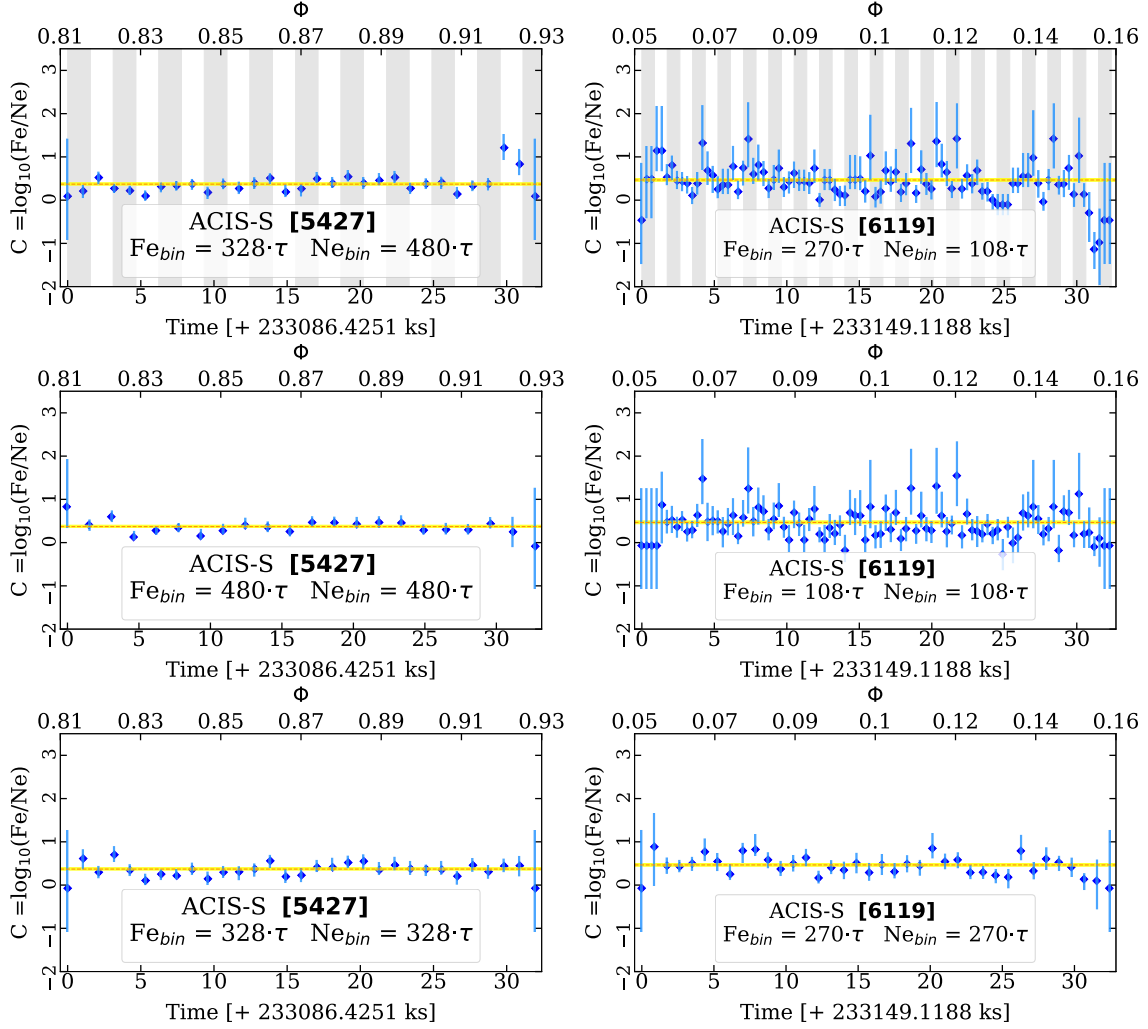


Figure 6.1: Color (C) graphs for the Fe1718 and bandNe pass bands for the observation IDs 5427 and 6119.

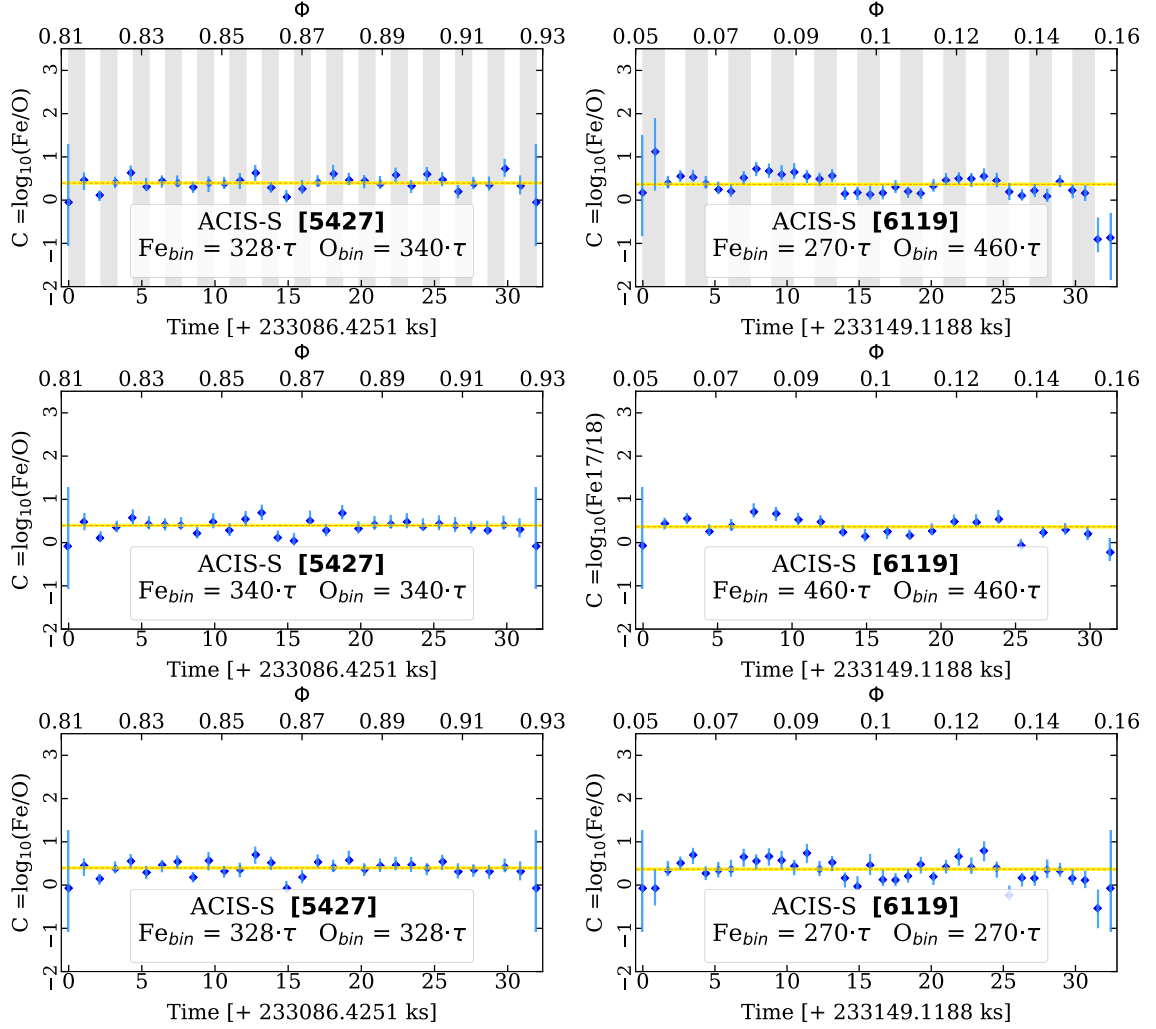


Figure 6.2: Color (C) graphs for the Fe1718 and bandO pass bands for observation IDs 5427 and 6119.

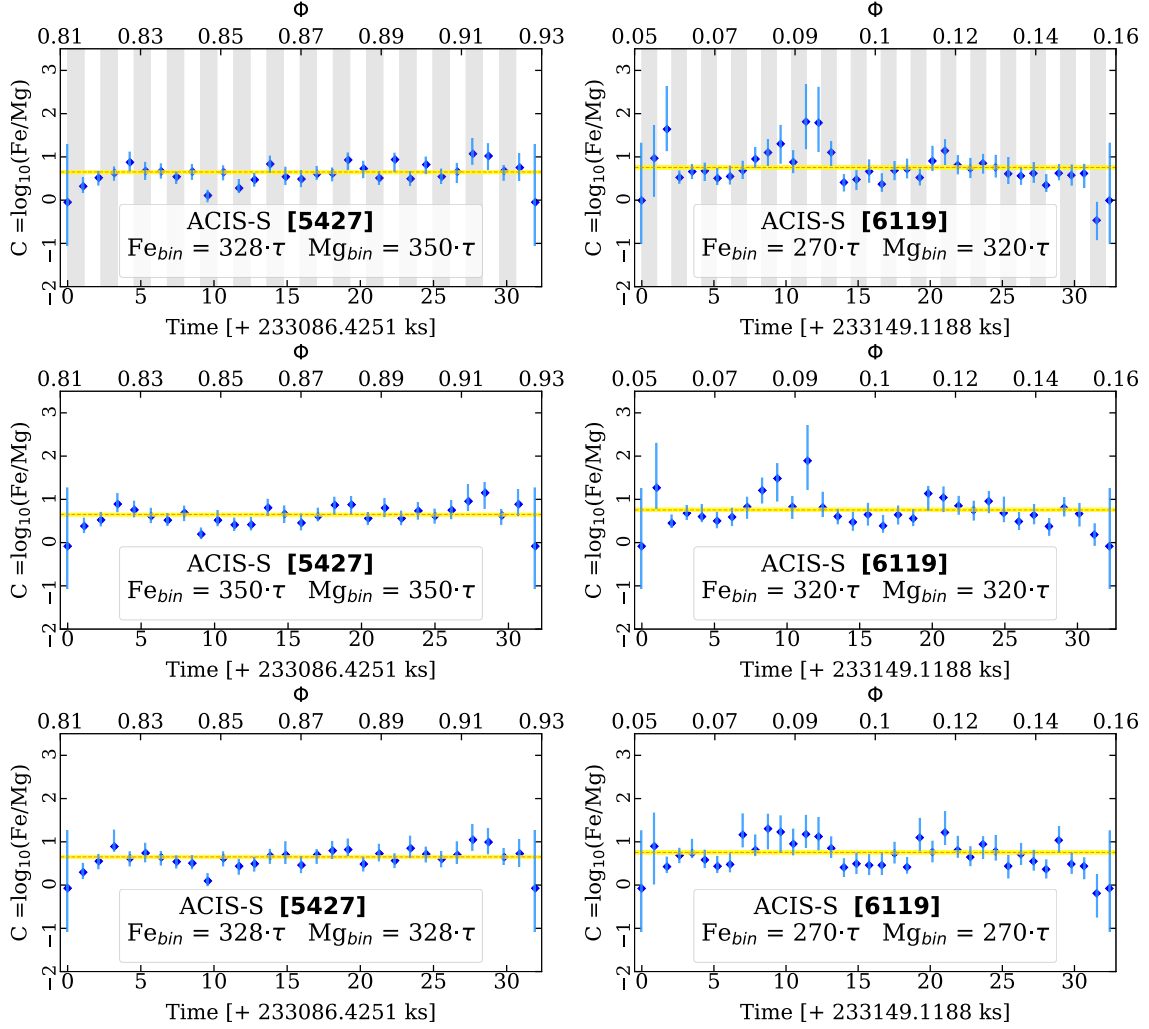


Figure 6.3: Color (C) graphs for the Fe1718 and bandMg pass bands for observation IDs 5427 and 6119.

A.2 Hardness Ratios and Color for the Chandra pass bands

We have also analysed the Hardness Ratios and Color for the Chandra pass bands, as shown for observation ID 6119 in Figs. 6.4 and 6.5.

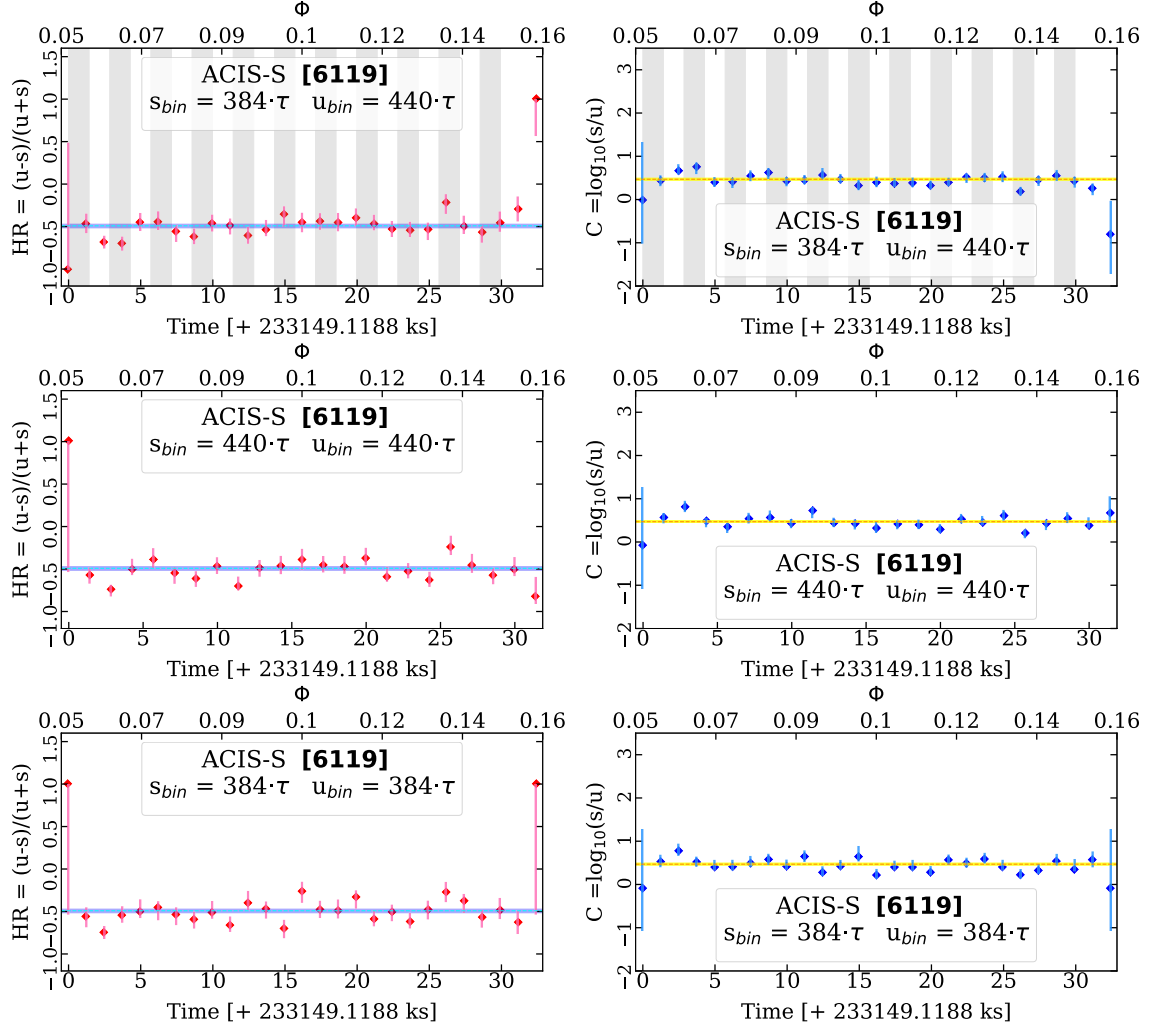


Figure 6.4: Hardness Ratio (HR) and Color (C) graphs for the Soft and Ultrasoft pass bands.

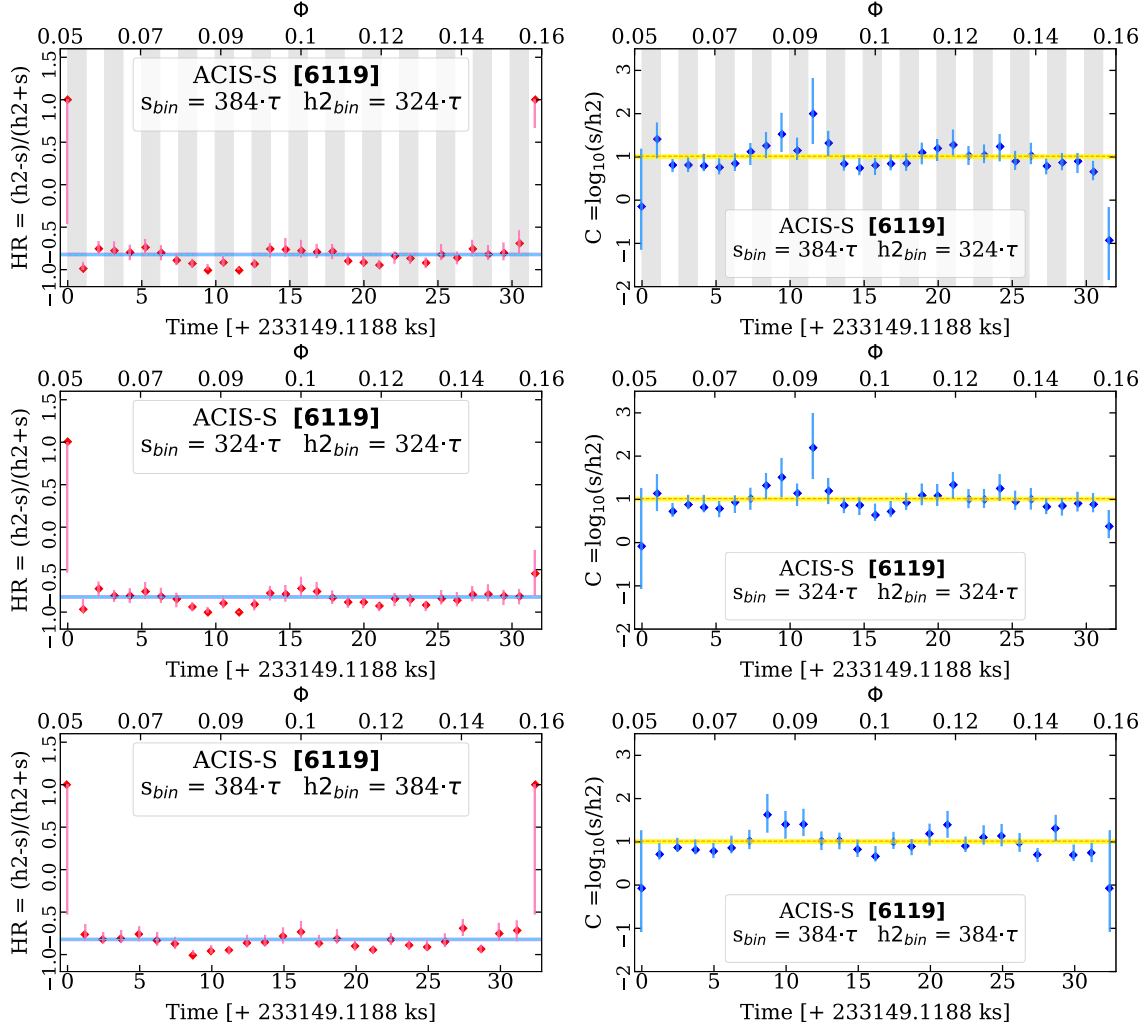


Figure 6.5: Hardness Ratio (HR) and Color (C) graphs for the Soft and Medium + Hard pass bands.